Slip Control for IWM Vehicles Based on Hierarchical LQR

Binh-Minh Nguyen[a], Shinji Hara[b], Hiroshi Fujimoto[c], and Yoichi Hori[c]
[a] Department of Information Physics and Computing, the University of Tokyo, Japan (binh_minh_nguyen@ipc.i.u-tokyo.ac.jp)
[b] Research and Development Initiative, Chuo University, Japan (shinji_hara@ipc.i.u-tokyo.ac.jp)
[c] Department of Advanced Energy, the University of Tokyo, Japan (fujimoto@k.u-tokyo.ac.jp, hori@k.u-tokyo.ac.jp)

***Abstract* –A proper dynamical model with the physical interconnection is necessary to accurately capture the slip phenomena of in-wheel-motored vehicles, since the wheels interact with each other through the vehicle body to make up the vehicle motion. Considering the uptrend in the number of in-wheel-motors, this paper proposes a way to effectively model the slip phenomena as a multi-agent dynamical system. A hierarchical LQR for time-varying interconnected system, which can significantly reduce the design burden, is presented for managing the wheel slip ratios properly, and the effectiveness of our proposed method is verified by both simulations and experiments.**

***Index Terms* - Electric vehicle, In-wheel-motor, Traction control, Slip ratio, Hierarchical LQR, Multi-agent dynamical system.**

1. Introduction

In order to protect our planet and tackle the global warming, electric vehicles (EVs) become an important solution to replace the gasoline vehicle. Supported by related technologies like motor design and control, supercapacitor, wireless power transfer, EVs have grown up considerably all over the world. Especially, the practical application of in-wheel-motor (IWM) allows many revolutionary developments in the field of EV. A remarkable benefit is that IWM enables driving/braking torque to be generated with fast response and high precision at individual wheels. This makes IWM-EVs to be a novel and advanced motion control system in comparison with the conventional EVs and the internal combustion engine vehicles [1]. Various control schemes have been proposed based on the advantages of IWM, such as direct yaw moment control [2] and range extension control [3]. This paper will focus on the most primary issue of IWM-EV control. It is called traction control, which generates the proper motion between the vehicle and the road surface.

Through literature review, traction control of EV can be categorized by three main groups, namely (I) slip ratio control, (II) wheel velocity control, and (III) wheel driving force control, as listed in TABLE 1.

Slip ratio control is the most popular and classical. Considering the nonlinearities in the tire-road friction characteristics, nonlinear control, especially the sliding-mode-control, becomes the dominant scheme in this group [4], [5], [6], [7], [8]. It always faces the chattering problem in sliding mode control, although it is very effective. On the other hand, some researchers tried to linearize the slip ratio dynamics to design a linear controller [9], [10]. Due to the complexity of linearization, this scheme has not been favored in the research community.

Wheel velocity control is mainly based on a popular robust control scheme using "disturbance observer" [11]. By introducing the zero-slip-model for wheel rotational dynamics, traction of EV can be achieved through a model following control [12]. This scheme can be integrated with direct yaw moment control to improve the stability of vehicle motion on snowy road [13]. Another scheme in this group is traction control based on maximum transmissible torque estimation (MTTE) developed by Yin *et al* [14]. The last one in this group, reference [15], introduced a slip ratio control method through controlling the wheel velocities directly. The wheel velocity control group has two advantages; it is very simple to implement, and it usually does not require the measurement of vehicle body's velocity. However, it cannot assure the optimal traction, such as optimal slip ratio at each wheel.

Thanks to the capability of driving force estimation with IWMs, feedback control of wheel driving force has been realized in [16], [17], and [18]. This method is very convenient to combine with higher layer motion control, such as yaw rate control or range extension control. Although the impressing experiment results were attained, this scheme is not really easy to implement. The driving force control configuration is quite complex. It includes the inner loops for managing the wheel velocities, and the outer loops for controlling the virtual variable $y = \lambda/(1-\lambda)$, where λ is the slip ratio.

In recent years, the research society has observed the uptrend in the number of IWMs installed in the EVs. For instance, France Army has developed an armored vehicle DPE6x6 driven by six independent motors [19]. A research group in Keio University introduced an electric vehicle installed with eight IWMs [20]. Many multi-in-wheel-motor EV prototypes have been produced and tested around the world, such as the experimental model of Hori-Fujimoto group [17] and Abe group [21]. Thanks to this trend, human beings are benefited with the more powerful and more flexible vehicles. On the other hand, the IWM-EV can be seen a multi-agent system in which each local agent is a locally controlled wheel (Fig. 1(a)). Therefore, EV system design becomes an actual new challenge. Luckily, the state-of-the-art of multi-agent systems can be applied to EV traction control.

TABLE 1
LITERATURE REVIEW OF TRACTION CONTROL METHODS FOR IN-WHEEL-MOTORED VEHICLES

Group No.	Objective	Scheme	Comments	Reference No.
(I)	Wheel slip ratio	Nonlinear control (sliding-mode)	- Chattering problem - Physical interaction is neglected	[4], [5], [6], [7], [8]
		Linear control by linearizing the slip ratio dynamics	- Linearization is complex - Physical interaction is neglected	[9], [10]
(II)	Wheel velocity	Zero-slip-model following control	- Optimal traction is not assured - Physical interaction is neglected	[12], [13]
		Maximum transmissible torque estimation	- Optimal traction is not assured - Physical interaction is neglected	[14]
		Direct wheel velocity control	- The control system is simple to implement - The physical interaction is neglected	[15]
(III)	Wheel driving force	Direct driving force control	- Driving force dynamics is poorly modelled - Physical interaction is neglected	[16]
		Driving force control based on wheel velocity and virtual variable control	- Control configuration is complex - Physical interaction is neglected	[17], [18]

The literature review reveals that traction control might be designed by the glocal (global/local) framework proposed by Hara *et al* [22]. Glocal control has been shown an effective way to analyze multi-agent dynamical systems such as gene-regulatory network [23] and platoon-car [24]. In the glocal control theory family, hierarchical linear quadratic regulator (H-LQR) [25], [26], [27], [39] is a scheme to design the optimal controller for complex dynamical system. The key of H-LQR is to utilize some special features in the structure of the system to reduce the design cost as well as the real time computational complexity.

From the view point of glocal control theory, several critical issues still remain in traction control of IWM-EVs. Firstly, all the aforementioned works [4] ~ [18] neglect the physical interaction among the wheel rotational dynamics. For instance, in [17], Maeda *et al* introduced a driving force control system for the EV driven by four IWMs. The system is merely the combination of four decoupled force control loops. In [4], Nam *et al* modeled the single wheel dynamics without any relevant to the others and designed a sliding-mode controller independently for each wheel. In fact, the physical interaction exists since the wheels are installed to the mechanical structure of the car body, and they cooperate with each other to generate the motion of the car body. As clarified by an application of "generalized frequency variable" to EV [28], neglecting physical interaction might results in instability phenomena of the overall system. Even if each wheel's control loop is stable, this does not assure the stability of the EV system as a whole. Therefore, it is essential to model the EV as an interconnected system to properly design the traction control. Secondly, following the uptrend in the number of IWMs, designing the EV traction control system becomes more and more complex. Increasing the number means increasing the order of the interconnected system, the implementation effort, and the computational time.

This paper tackles the above issues by focusing on the wheel slip ratio control as a case study. Firstly, it shows that the slip ratio dynamics can be modeled as a time-varying interconnected system. Since the H-LQR in the previous works ([25] ~ [27], [39]) only deals with time-invariant system without interconnection, a new time-varying H-LQR will be developed for traction control of IWM-EV. The H-LQR

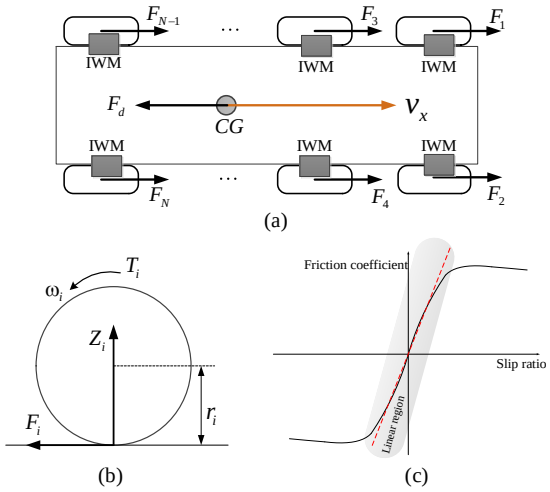

Fig.1. Modeling of IWM-EV:
(a) Vehicle body, (b) Rotation of single wheel, (c) relationship between friction coefficient and slip ratio.

includes two layers, the lower-layer designed for the local agent dynamics, and the upper-layer that takes into account the physical interaction. It is only required to solve the Riccati equation for each local sub-system no matter what the number of IWMs installed into the car body. Then, the control gains are optimally obtained through a suitable procedure.

The original idea of this paper was presented at SICE ISCS 2016 [29], which showed how to apply the H-LQR method to the driving force control of EVs and demonstrated its effectiveness only by simulations. This paper extends the H-LQR method to the slip ratio control with complete design procedure and confirms the effectiveness by both simulations and experiments. Besides that, simulations and experiments of other slip ratio control methods are conducted for clear discussion.

The reminder of the paper is organized as follows. Vehicle dynamics modelling are presented in Section 2. In Section 3, the motivation of this paper is introduced by discussing the disadvantage of neglecting physical interaction. Section 4 clarifies the assumptions and problem setting for traction control design in this paper. Section 5 is to establish a systematic design procedure for H-LQR which can be applied

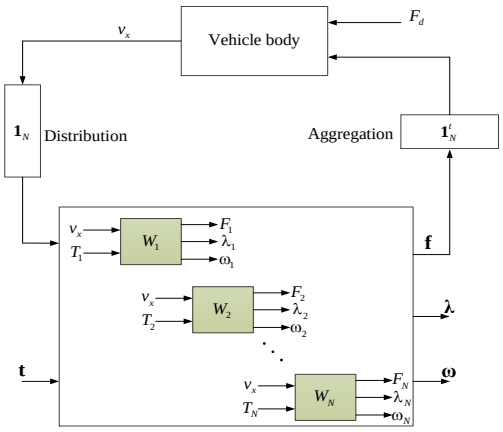

Fig.2. Block diagram of IWM-EV.

to wheel slip ratio control. Simulation and experimental results are shown in Section 6 and Section 7 in order to demonstrate the effectiveness of the proposed method with concrete control implementation. Finally, concluding remarks are given in Section 8.

2. Fundamental dynamics of electric vehicles

It is essential to understand the EV dynamics to design the traction control system. The dynamics depends on the structure of the EV which is various in many aspects. This paper only examines the longitudinal motion of the IWM-EV illustrated in Fig. 1(a). The body shape is rectangular, the number of wheels (N) is an even number, and the wheels are distributed symmetrically about the front-rear center line of the vehicle. Besides that, m is the vehicle mass; v_x is the longitudinal velocity; J_i and r_i are the inertia and the radius of the ith wheel; T_i, F_i, and Z_i are the motor torque, the longitudinal or driving force, and the vertical force acting at the ith wheel, respectively and ω_i is the ith wheel's rotational velocity. Air resistance and rolling resistance are summarized as F_d, and they can be considered as the unknown disturbance of the vehicle system. By Newton law of motion, the longitudinal dynamics of the vehicle is expressed as:

$$m\dot{v}_x = \sum_{i=1}^{N} F_i - F_d \tag{1}$$

The rotational motion of the ith wheel is described as

$$J_i\dot{\omega}_i = T_i - r_i F_i \tag{2}$$

Besides that, the wheel slip ratio λ_i is defined by

$$\lambda_i = \frac{\omega_i r_i - v_x}{\max\{\omega_i r_i, v_x, \varepsilon\}} \tag{3}$$

where ε is a small number to avoid division-by-zero.

The driving force is decided by the vertical force and the road friction coefficient. The vertical force frequently changes due to the vehicle acceleration and the height of the center of gravity. On the other hand, there exists a nonlinear relationship between the road friction coefficient and the slip ratio as shown in Fig. 1(c). Many models are proposed to capture the nonlinearity of the curve $\mu_i(\lambda_i)$, such as the famous "magic formula" proposed by Pacejka [30]. Consequently, the

Fig.3. Pickup vehicle model provided by Carsim.

TABLE 2
SPECIFICATION OF THE SIMULATION VEHICLE MODEL

Vehicle mass (no load)	1998 kg
Load capacity	0 ~ 2000 kg
Track-width of front and rear wheel	1.9 m
Distance from front wheel axle to CG	1.4 m
Distance from rear wheel axle to CG	2.6 m
Height of CG	0.797 m
Unloaded tire radius	0.402 m
Wheel spin inertia	3.2 kgm^2
Maximum torque of each wheel	5000 N.m

IWM-EV is a nonlinear system with the block diagram depicted in Fig. 2, where the vectors with size N are defined as

$$\mathbf{1}_N = [1 \;\; 1 \;\; \cdots \;\; 1]^t, \mathbf{t} = [T_1 \;\; T_2 \;\; \cdots \;\; T_N]^t, \mathbf{f} = [F_1 \;\; F_2 \;\; \cdots \;\; F_N]^t$$

$$\boldsymbol{\lambda} = [\lambda_1 \;\; \lambda_2 \;\; \cdots \;\; \lambda_N]^t, \boldsymbol{\omega} = [\omega_1 \;\; \omega_2 \;\; \cdots \;\; \omega_N]^t$$

As shown in Fig. 2, the IWM-EV system includes N local subsystem $\{W_1, W_2, \ldots, W_N\}$ physically interconnected via the vehicle body dynamics with the aggregation and distribution channels. To generate the traction torque **t**, one might choose to control the driving force **f**, slip ratio **λ**, or wheel velocity **ω**.

3. Motivating example with simulations

This section examines dynamic behavior in traction control method that neglects the physical interaction among the local sub-systems as depicted in Fig. 2 in order to clarify the motivation of this paper.

3.1. Vehicle models

It is essential to build an accurate simulation model to verify the slip ratio control. For this reason, this paper utilized Carsim – a standard software for simulating the vehicle dynamics [31]. By using Carsim, it is convenient to test the control algorithm with various environmental conditions, including the extreme conditions which are dangerous to realize in actual experiment.

Simulations in this paper were conducted based on a pickup vehicle model shown in Fig. 3. Originally, Carsim library only provides the vehicle of gasoline type. However, the IWM block

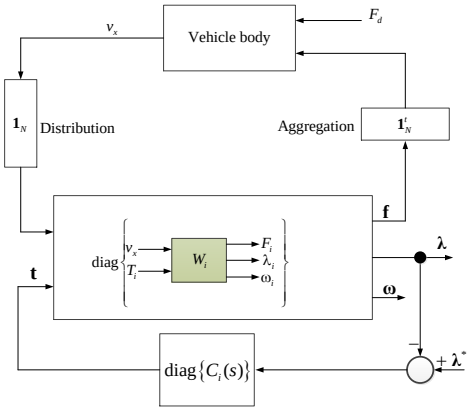

Fig.4. Block diagram of slip ratio control system based on linearization of the slip ratio dynamics.

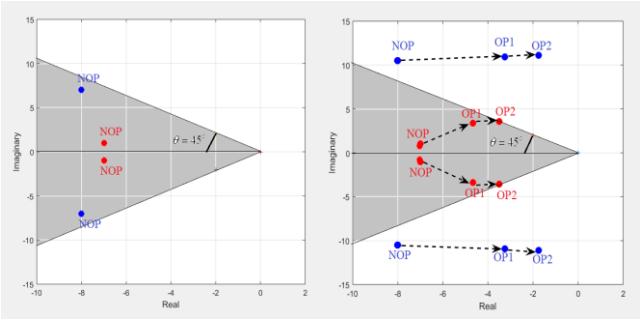

(a) (b)

Fig.5. Pole placement for slip ratio control: (Case 1: Red-dot, Case 2: Blue-dot.) (a) Pole-placement of the local subsystem at NOP. (b) Actual pole of the overall system at different OPs.

can be modelled in Matlab/Simulink, and the output torques of IWMs are sent to Carsim model through the imports namely IMP_MYUSM_*. The notation * represents the IWM position (L1, L2, R1, R2). By this way, a pickup EV model driven by four independent IWMs (N = 4) is established. Several important parameters of the vehicle model are summarized in TABLE 2. A typical example of the nonlinear relationship between driving force and slip ratio is presented in Appendix 1.

3.2. Traction based on linearizing the slip ratio dynamics

If each IWM is provided a local controller $C_i(s)$, the slip ratio control system is constructed as in Fig. 4, where λ^* is the reference slip ratio. In this sub-section, the local controller $C_i(s)$ is designed through the linearization of the slip ratio dynamics. Consider the driving mode with $\max\{\omega_i r_i, v_x, \varepsilon\} = \omega_i r_i$ and calculate the derivative of (3) with the respect to (1) and (2), then the slip ratio dynamics is given by

$$\dot{\lambda}_i = -\frac{r_i}{J_i\omega_i}F_i - \frac{\dot{\omega}_i}{\omega_i}\lambda_i + \frac{1}{J_i\omega_i}T_i - \frac{1}{mr_i\omega_i}\sum_{j=1}^{N}F_j \tag{4}$$

In (4), substituting $F_i = S_i\lambda_i$, where S_i is the driving stiffness calculated by linearizing the tire-force characteristics. Then, let the rotational velocity and its derivative be the time-varying parameters, the following dynamics is obtained

$$\dot{\lambda}_i = -\left(\frac{\dot{\omega}_i}{\omega_i} + \frac{r_i S_i}{J_i\omega_i}\right)\lambda_i + \frac{1}{J_i\omega_i}\left(T_i - T_{p,i}\right) \tag{5}$$

where the physical interaction is expressed by

$$T_{p,i} = \frac{J_i}{mr_i}\sum_{j=1}^{N}S_j\lambda_j = \frac{J_i}{mr_i}\mathbf{S}^t\boldsymbol{\lambda}$$

with the vector of driving stiffness $\mathbf{S} = \begin{bmatrix} S_1 & S_2 & \dots & S_N \end{bmatrix}^t$

The local transfer function from T_i to λ_i is given by

$$P_i(s) = \frac{h_i}{s+\rho_i} \quad \rho_i = \left(\frac{\dot{\omega}_i}{\omega_i} + \frac{r_i S_i}{J_i\omega_i}\right), \; h_i = \frac{1}{J_i\omega_i} \tag{6}$$

if the physical interaction term is neglected from (5). The transfer function of the local subsystem is then written as

$$H_i(s) = \frac{P_i(s)}{1 + C_i(s)P_i(s)}$$

Calculate the nominal parameters ρ_n and h_n at the nominal operating point (NOP) $\{\omega_n; \dot{\omega}_n\}$. Let p_1 and p_2 be two designed poles of the local subsystem at NOP. Then $C_i(s)$ can be designed as a PI controller. The controller's gains are calculated as follows:

$$\begin{cases} K_p = p_1 p_2 / h_n \\ K_i = \left(-(p_1 + p_2) - \rho_n\right)/h_n \end{cases} \tag{7}$$

To the best of our knowledge, all most the conventional slip ratio control design schemes only focused on stabilizing the local dynamics given by $H_i(s)$. The limitation of such schemes will be discussed in the following sub-section.

3.3. Motivating example 1

As shown in Fig. 3, from an initial point in the high friction road surface (μ = 0.8), the vehicle accelerated and entered the low friction road surface (μ = 0.2). The reference slip ratio is set as λ^* = 0.1 to maintain the safe traction. In this test, the load is set as 5% of the maximum capacity. An NOP is selected as $\{\omega_n = 40rad/s;\ \dot{\omega}_n = 400rad/s^2\}$. The local PI controller $C_i(s)$ is designed using (8), such that the poles of the local subsystem are placed at the left half complex plane. A reasonable way for placing the poles of $H_i(s)$ is the shaded region in Fig. 5(a) with the angle θ = 45º. Two test cases are as follows:

- Case 1: The poles of $H_i(s)$ are placed at -7 ± 1j at NOP (Red dots).
- Case 2: The poles of $H_i(s)$ are placed at -8 ± 7j at NOP (Blue dots).

If the physical interaction term $T_{p,i}$ is addressed, the total system included N local subsystem $H_i(s)$ interconnected through the interaction matrix G defined as

$$G = -diag\left\{\frac{J_i}{mr_i}\right\}\mathbf{1}_N\mathbf{S}^t \tag{8}$$

As can be seen from (9), matrix G relies on the physical parameters of the vehicle. Following the theory of "generalized frequency variable" [32], the performance of the overall system $\Sigma(G, \{H_i(s)\})$ should be determined by both local sub-system's transfer function $H_i(s)$ and matrix G. For simplicity, $\{H_i(s)\}$ are assumed to be homogeneous. Fixing the control gains obtained at the NOP, the poles $\Sigma(G, \{H_i(s)\})$ are calculated at different operating points in the slip scenario, i.e.:

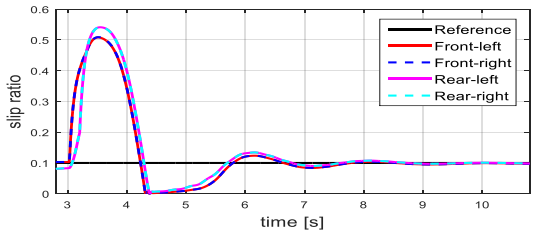

(a) Case 1 (normal operation)

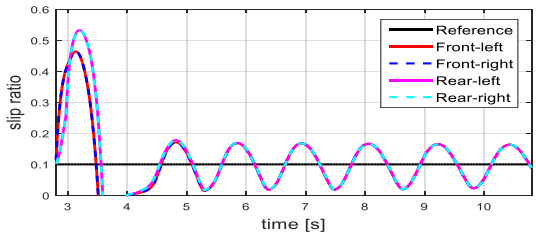

(b) Case 2 (vibration)

Fig.6. Simulation of Example 1.

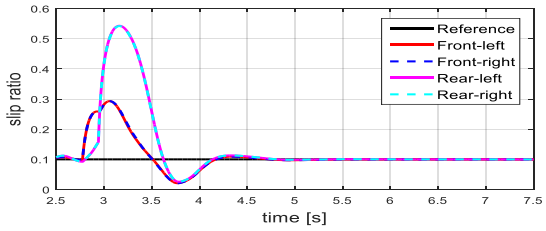

Fig. 7. Simulation of Example 2 – large gap due to load transfer.

OP1: $\{ \omega_{o,i} = 60 rad/s;\ \dot{\omega}_{o,i} = 300 rad/s^2 \}$

OP2: $\{ \omega_{o,i} = 80 rad/s;\ \dot{\omega}_{o,i} = 200 rad/s^2 \}$

Since the vehicle has 4 wheels, $\Sigma(G, \{H_i(s)\})$ has 8 poles. The poles are organized by two groups, each consists of four poles, shown in Fig. 5(b). The poles move from NOP to OP1, then to OP2 following the arrow direction.

In Case 1, all the poles of $\Sigma(G, \{H_i(s)\})$ are remained inside the shaded region with NOP and OP1. They slightly cross the shaded region's boundary at OP2. Basically, the pole placement in Case 1 is acceptable. However, the poles move towards the point (0, 0) with the increasing imaginary parts as the wheel velocity increases. This might degrade the system performance, especially on extreme scenarios as high velocity and/or severe load transfer among the wheels.

In Case 2, all the poles of $\Sigma(G, \{H_i(s)\})$ are not remained in the shaded region. Instead, they are moved towards the imaginary axis faster in comparison with Case 1. Moreover, the imaginary parts increase as the wheel velocity increases from OP1 to OP2. This trend is quite dangerous since the EV system becomes more sensitive to the vibration, especially when operating at high velocity.

In Case 1, the slip ratios finally follow the reference value smoothly, as shown in Fig. 6(a). On the other hand, oscillated phenomena can be seen in Fig. 6(b) for Case 2. As the above discussion, the wheel slip ratios and motor torques experience the unwanted vibration. This phenomenon introduces the bad influence to motion control performance and degrades the driver's comfort.

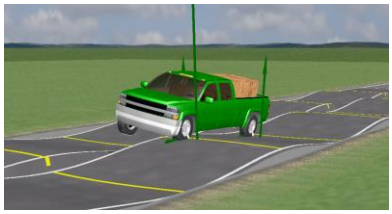

(a) Non-flat surface in Carsim

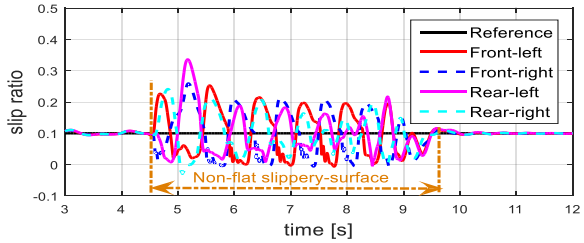

(b) Slip ratio control

Fig. 8. Simulation of Example 3 (non-flat road surface between 4.5 and 9.5 seconds).

3.4. *Motivating example 2*

In this example, the environmental setting is similar to Example 1, but the load of the vehicle is increased to 50% of the maximum capacity. With the same NOP as Example 1, the poles of the local subsystem are assigned at -10 ± 1*j* to achieve faster tracking with the reference value. However, the slip ratios can be divided by two groups, namely, front-wheel and rear-wheel (Fig. 7). There exists a large gap between two groups as the vehicle enters the slippery surface. This gap can be explained as the result of load transfer among the wheels.

3.5. *Motivating example 3*

Using Carsim Library, a test course, namely "Chassis twist road sine wave" was prepared as in Fig. 8(a) with low friction coefficient (μ = 0.2). The PI-based-slip ratio controller is similar to that of Example 2. The vehicle has to carry a load of 1000 kg or 50% of its maximum capacity. Thus, the vertical force at each wheel changes frequently and sharply when the vehicle runs on the non-flat surface between 4.5 and 9.5 seconds. This varies the driving stiffness, and consequently, the interconnection matrix *G*. As a result, actual slip ratios deviate considerably from the reference value (Fig. 8(b)).

3.6. *Discussion*

From the above examples, a design method which only stabilizes the local sub-system does not assure the system's good performance globally. It is also a non-trivial task to stabilize the EV system by fixed control gains. Besides that, a controller which neglects the physical interaction cannot reduce the gap of slip ratios between different wheels due to the load transfer. Moreover, no study has been proposed to guarantee the stability of the overall system for every operating point.

The motivating examples show that the IWM-EV should be considered as a type of multi-agent system and the physical interaction should be treated properly. The next section will introduce a model of IWM-EV dynamics that captures the physical interaction. Then, a new design procedure that reducing the burden of computation is proposed.

4. Hierarchical modeling

Firstly, this section shows that the vehicle dynamics can be approximately represented using a linear interconnected model with time-varying parameters. Then, this section proposes several assumptions and a problem setting, which are suitable for the practical design of traction control.

4.1. Interconnected model of vehicle dynamics

The slip ratio dynamics is expressed as (4) in the driving mode. Similarly, in the braking mode

$$\dot{\lambda}_i = -\frac{r_i^2}{J_i v_x} F_i - \frac{\dot{v}_x}{v_x}\lambda_i + \frac{r_i}{J_i v_x} T_i - \frac{1}{m v_x}\sum_{j=1}^{N} F_j \tag{9}$$

Commonly, the purpose of the traction control is to maintain the slip ratio at small values such that the road friction coefficient still has linear relationship with the slip ratio. For this reason and for the sake of control design based on state space representation, it is possible to use the first order dynamics model of the driving force represented by

$$\tau_i \dot{F}_i + F_i = \bar{F}_i = \mu_i(\lambda_i) Z_i \approx \left(S_i^* \lambda_i\right) Z_i = S_i \lambda_i \tag{10}$$

where τ_i is the relaxation time constant and S_i is the driving stiffness which is a parameter for capturing the linear region in Fig. 1(c) [33]. Here, S_i can be identified from IWM's torque and on-board sensor [34]. Equation (10) can be rewritten as

$$\dot{F}_i = -\frac{1}{\tau_i} F_i + \frac{S_i}{\tau_i}\lambda_i \tag{11}$$

Since the purpose of this paper is to control the slip ratio, the slip ratio and the driving force can be selected as the state variables. On the other hand, the vehicle velocity, the wheel velocity and their derivatives, can be considered as time-varying parameters. From (4), (9) and (11), the dynamical equation of the ith agent can be expressed in state space form as

$$\dot{\mathbf{x}}_i(t) = \mathbf{A}_{l,i}(t)\mathbf{x}_i(t) + \mathbf{B}_{l,i}\mathbf{u}_i(t) + \sum_{j=1}^{N}\mathbf{A}_{g,ij}(t)\mathbf{x}_j(t) \tag{12}$$

where

$$\mathbf{x}_i(t) = \begin{bmatrix} F_i(t) & \lambda_i(t) \end{bmatrix}^T,\ \mathbf{u}_i(t) = T_i(t)$$

The matrices of the dynamic equation (12) in the driving mode are expressed as

$$\mathbf{A}_{l,i}(t) = \begin{bmatrix} \frac{-1}{\tau_i} & \frac{S_i}{\tau_i} \\ \frac{-r_i}{J_i\omega_i} & \frac{-\dot{\omega}_i}{\omega_i} \end{bmatrix},\ \mathbf{A}_{g,ij}(t) = \begin{bmatrix} 0 & 0 \\ \frac{-1}{m r_i \omega_i} & 0 \end{bmatrix},\ \mathbf{B}_{l,i}(t) = \begin{bmatrix} 0 \\ \frac{1}{J_i\omega_i} \end{bmatrix}$$

In the braking mode, those matrices are given by

$$\mathbf{A}_{l,i}(t) = \begin{bmatrix} \frac{-1}{\tau_i} & \frac{S_i}{\tau_i} \\ \frac{-r_i^2}{J_i v_x} & \frac{-\dot{v}_x}{v_x} \end{bmatrix},\ \mathbf{A}_{g,ij}(t) = \begin{bmatrix} 0 & 0 \\ -\frac{1}{m v_x} & 0 \end{bmatrix},\ \mathbf{B}_{l,i}(t) = \begin{bmatrix} 0 \\ \frac{r_i}{J_i v_x} \end{bmatrix}$$

Equation (12) shows that the slip ratio and the driving force dynamics are modelled as a linear time-varying interconnected system. If the vehicle velocity and the wheel velocities are measurable, the matrices $\mathbf{A}_{l,i}(t)$, $\mathbf{A}_{g,ij}(t)$, and $\mathbf{B}_{l,i}(t)$ are available at every control period. Besides that, this model can be shared among all three groups in TABLE 1. One might use this model for the slip ratio control or the driving force control. In general, simple decentralized controllers cannot assure the optimality of the overall system due to the interaction term represented by $\mathbf{A}_{g,ij}(t)$. Theoretically speaking, one might utilize a standard MIMO control design, such as the LQR method. However, as the number of IWM increases, it is really hard to implement such standard LQR in real time application due to the considerable size of the system matrices and the huge computational efforts. Considering this issue, this paper will propose an H-LQR design procedure to effectively reduce the computational cost in the next section.

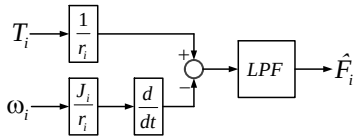

Fig.9. Driving force observer.

4.2. Assumptions and remarks

This sub-section clarifies four assumptions to be made and their remarks accordingly.

Assumption 1: All the state variables and time-varying parameters of the system (12) or their appropriate estimates are available.

Remark 1: With the **Assumption 1**, this paper only focuses on the controller design. When implementing the traction control system, driving force observer is utilized to obtain the driving force at each wheel. This observer was presented in many papers as [16], [17], and its structure is shown in Fig. 9 where LPF is a first-order low-pass-filter. Notice that the motor torque T_i is known accurately, and this is a remarkable merit of using IWM. Besides that, the wheel's rotational velocity is measurable using encoder installed at each wheel. To obtain the slip ratio, firstly the vehicle velocity is estimated using GPS and IMU [35]. Then, the slip ratio is calculated using the definition (3). Another way is to estimate the slip ratio directly [34]. The rotational acceleration of the wheel can be calculated as

$$\dot{\omega}_i(s) = \frac{s}{\rho s + 1}\omega_i(s) \tag{13}$$

where ρ is a small time constant which has two purposes. Firstly, it is used for realizing the derivative in real-time calculation. Secondly, it helps rejecting the high frequency noises in the measurement of wheel's rotational velocity. The detail of the state estimation procedure is not shown here, since this is not the main issue of this paper. See Appendix 2 for a brief explanation of a strategy for estimating the slip ratio.

Assumption 2: The sets of parameters $\{r_i, J_i, S_i, \tau_i, \omega_i, \dot{\omega}_i\}$ for i = 1, … , N are almost the same, and they can be represented by the normalized set $\{r_n, J_n, S_n, \tau_n, \omega_n, \dot{\omega}_n\}$.

Remark 2: Since the physical designs of the wheels are commonly identical, it is reasonable to assume that $r_i = r_n$, $J_i = J_n$, and $\tau_i = \tau_n$ for i from 1 to N. However, it is understandable that ω_i and $\dot{\omega}_i$ depends on the local road condition at each wheel, and S_i depends on the load transfer. This means the parameters $\{S_i, \omega_i, \dot{\omega}_i\}$ are not always the same in real-time

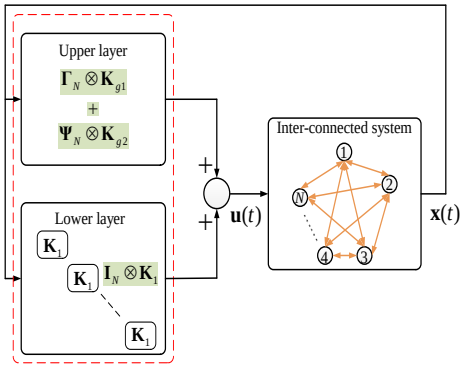

Fig. 10 Hierarchical LQR for interconnected system.

operation. But for the sake of simplicity in clarifying the idea of H-LQR, this paper first assumes that these parameters are not much different from wheel to wheel. For instance, if the local road conditions of the wheels are quite uniform, and if the slip ratio is maintained small, the wheel velocities are almost the same. The normalized velocity ω_n can be calculated as the average of all wheels' velocity. With **Assumption 2**, the system (12) becomes the combination of N homogeneous sub-systems and the H-LQR design procedure will be developed accordingly. Lately, by Carsim simulation, this paper will show that, H-LQR based on **Assumption 2** is still effective, even if the vehicle run on non-uniform road conditions with severe load transfer. Since H-LQR is a kind of feedback control, it can compensate the parameter difference among the local agents. Note that the design of H-LQR for heterogeneous system is still available as mentioned in [25] and [39], but the detail investigation of the heterogeneous system will be a part of our future works.

Assumption 3: This paper only presents the control design in driving mode.

Remark 3: The control designs for the driving mode and braking mode are almost the same. For the sake of simplicity, only the driving case is presented.

Assumption 4: The controller is turned-on if the vehicle velocity is bigger than a threshold.

Remark 4: If the vehicle velocity is closed to zero, the matrices $A_{l,i}(t)$, $A_{g,ij}(t)$, and $B_{l,i}(t)$ are unrealized. Thus, the EV system operates the traction control based on the model (12) if the vehicle velocity is bigger than a certain threshold v^*. If the vehicle velocity is smaller than v^*, the vehicle is only accelerated by the driver command.

4.3. Time-varying hierarchical modeling

With **Assumption 2**, the dynamics of the ith sub-system is

$$\dot{\mathbf{x}}_i(t) = \mathbf{A}_1(t)\mathbf{x}_i(t) + \mathbf{B}_1\mathbf{u}_i(t) + \sum_{j=1}^{N}\mathbf{A}_2(t)\mathbf{x}_j(t) \tag{14}$$

where the state matrices are obtained using the normalized parameter set. In acceleration mode, they are calculated as

$$\mathbf{A}_1(t) = \begin{bmatrix} \dfrac{-1}{\tau_n} & \dfrac{S_n}{\tau_n} \\ \dfrac{-r_n}{J_n\omega_n} & \dfrac{-\dot{\omega}_n}{\omega_n} \end{bmatrix}, \mathbf{A}_2(t) = \begin{bmatrix} 0 & 0 \\ \dfrac{-1}{mr_n\omega_n} & 0 \end{bmatrix}, \mathbf{B}_1(t) = \begin{bmatrix} 0 \\ \dfrac{1}{J_n\omega_n} \end{bmatrix}$$

From (14), the dynamical system for traction control is shown to be a time-varying interconnected system expressed as (15) in which the system matrices can be described using Kronecker product $\otimes$:

$$\dot{\mathbf{x}}(t) = \mathbf{A}(t)\mathbf{x}(t) + \mathbf{B}(t)\mathbf{u}(t) \tag{15}$$

where

$$\mathbf{A}(t) = \mathbf{I}_N \otimes \mathbf{A}_1(t) + \mathbf{\Gamma}_N \otimes \mathbf{A}_2(t) \tag{16}$$

$$\mathbf{B}(t) = \mathbf{I}_N \otimes \mathbf{B}_1(t) \tag{17}$$

$$\mathbf{\Gamma}_N = \mathbf{1}_N\mathbf{1}_N^T \tag{18}$$

with $\mathbf{x}(t) = \begin{bmatrix}\mathbf{x}_1^T(t) & \dots & \mathbf{x}_N^T(t)\end{bmatrix}^T$ and $\mathbf{u}(t) = \begin{bmatrix}\mathbf{u}_1^T(t) & \dots & \mathbf{u}_N^T(t)\end{bmatrix}^T$

5. Hierarchical design procedure

This section provides a method of hierarchical LQR control for the class of interconnected system represented by (15), where the time stamping "t" is eliminated due to the limitation of paper space.

5.1. Problem formulation

The LQR controller of the system (15) can be obtained by minimizing the quadratic cost function expressed as

$$\mathbf{J} = \int_{t_o}^{t_f}\mathbf{x}^T\mathbf{Q}\mathbf{x}dt + \int_{t_o}^{t_f}\mathbf{u}^T\mathbf{R}\mathbf{u}dt + \mathbf{x}_f^T\mathbf{H}\mathbf{x}_f \tag{19}$$

where t_0 is the initial time, t_f is the finished time. **Q** and **S** are symmetric positive semidefinite matrices, and **R** is strictly symmetric positive definite matrix. **Q**, **H**, and **R** are used to penalize the transient state deviation, the final state, and the control effort, respectively. This paper assumes standard controllability and observability conditions satisfy for the problem setting. Then, from the literature of LQR theory, the optimal feedback gain is given by

$$\mathbf{K} = -\mathbf{R}^{-1}\mathbf{B}^T\mathbf{P} \tag{20}$$

where **P** is the unique positive definite solution of the differential Riccati equation given by

$$\dot{\mathbf{P}} + \mathbf{P}\mathbf{A} + \mathbf{A}^T\mathbf{P} - \mathbf{P}\mathbf{B}\mathbf{R}^{-1}\mathbf{B}^T\mathbf{P} + \mathbf{Q} = \mathbf{0} \tag{21}$$

that satisfies the boundary condition

$$\mathbf{P}_f := \mathbf{P}(t_f) = \mathbf{H} \tag{22}$$

Equation (21) with boundary condition (22) can be solved backwards in time, or by using the Hamiltonian established from the system model. Even though, the conventional design procedure is unsuitable for the large scale and complex system, i.e: N is a big number. Thus, this study is motived by the idea of H-LQR controller presented in [25], [26], [27] and [39]. However, there methods are only applicable for time-invariant systems. Therefore, it is required to develop a new design procedure for the class of system (15).

Following [25], this paper proposes an optimal control method based on time-varying LQR which gives the optimal feedback gain of the form

$$\mathbf{K} = \mathbf{I}_N \otimes \mathbf{K}_1 + \mathbf{\Gamma}_N \otimes \mathbf{K}_{g1} + \mathbf{\Psi}_N \otimes \mathbf{K}_{g2} \tag{23}$$

by appropriate choices of the weighting matrices. As shown in Fig. 10, the feedback gain **K** consists of three terms, and each term is a Kronecker product of two matrices of which the first matrix corresponds to the physical meaning and/or the required

control performance as well as the feedback structure. The first term relates to the lower layer with the local feedback gain $\mathbf{K}_1$ for improving the control performance against local disturbances such as small road surface changes, because the first matrix is the identity matrix. The second term belongs to the upper layer with gain $\mathbf{K}_{g1}$, which is for tracking performance on the car velocity by considering the physical interconnection represented by $\mathbf{\Gamma}_N$. It is possible to introduce an extra terms, e.g. the third term in (23), to improve some other global performances. For instance, considering a four-wheel-vehicle, to reduce the imbalance of the left and right wheels, one of natural selections of positive semidefinite matrix $\mathbf{\Psi}_N$ is expressed as

$$\mathbf{\Psi}_4^{left-right} = \begin{bmatrix} \varphi_{left} & 0 \\ 0 & \varphi_{right} \end{bmatrix} \otimes \begin{bmatrix} 1 & -1 \\ -1 & 1 \end{bmatrix}$$

On the other hand, the selection of the positive semidefinite matrix $\mathbf{\Psi}_N$ for reducing the imbalance between the front and rear wheels could be

$$\mathbf{\Psi}_4^{front-rear} = \begin{bmatrix} 1 & -1 \\ -1 & 1 \end{bmatrix} \otimes \begin{bmatrix} \varphi_{front} & 0 \\ 0 & \varphi_{rear} \end{bmatrix}$$

where φ_{left}, φ_{right}, φ_{front} and φ_{rear} are non-negative weights. Note that the bigger weight of $\varphi_{\#}$ leads to much more balance.

5.2. Hierarchical LQR design procedure

The hierarchical control structure is shown in Fig. 8. In order to get an optimal feedback gain of the form (23), the weighting matrices are selected as:

$$\mathbf{Q} = \mathbf{I}_N \otimes \mathbf{Q}_1 + \mathbf{\Gamma}_N \otimes \mathbf{Q}_{g1} + \mathbf{\Psi}_N \otimes \mathbf{Q}_{g2} \tag{24}$$

$$\mathbf{R}^{-1} = \mathbf{I}_N \otimes \mathbf{R}_1^{-1} + \mathbf{\Gamma}_N \otimes \mathbf{R}_{g1}^{-1} + \mathbf{\Psi}_N \otimes \mathbf{R}_{g2}^{-1} \tag{25}$$

$$\mathbf{H} = \mathbf{I}_N \otimes \mathbf{H}_1 \tag{26}$$

where the matrices ($\mathbf{Q}_1$, $\mathbf{R}_1$, $\mathbf{H}_1$) are set for the lower layer, ($\mathbf{Q}_{g1}$, $\mathbf{R}_{g1}$) and ($\mathbf{Q}_{g2}$, $\mathbf{R}_{g2}$) are set for the upper layer. This paper will prove that the following three-step design procedure provides one of the right ways.

Step 1 (Lower layer)

Select the weighting matrices ($\mathbf{Q}_1$, $\mathbf{R}_1$, $\mathbf{S}_1$) such that $\mathbf{Q}_1$ and $\mathbf{S}_1$ are positive semidefinite, and $\mathbf{R}_1$ is strictly positive definite. Then, solve the differential Riccati equation

$$\dot{\mathbf{P}}_1 + \mathbf{P}_1\mathbf{A}_1 + \mathbf{A}_1^T\mathbf{P}_1 - \mathbf{P}_1\mathbf{B}_1\mathbf{R}_1^{-1}\mathbf{B}_1^T\mathbf{P}_1 + \mathbf{Q}_1 = \mathbf{0} \tag{27}$$

with the boundary condition

$$\mathbf{P}_1(t_f) := \mathbf{P}_{1f} = \mathbf{H}_1 \tag{28}$$

Step 2 (Upper layer)

Select the positive semidefinite matrix $\mathbf{\Psi}_N$ and the positive definite matrices $\mathbf{R}_{g1}$ and $\mathbf{R}_{g2}$ to obtain the weighting matrix $\mathbf{R}$ as in (25). Then, the two matrices $\mathbf{Q}_{g1}$ and $\mathbf{Q}_{g2}$ are set as following such that $\mathbf{Q}_{g1}$ is positive semidefinite:

$$\mathbf{Q}_{g1} = \mathbf{P}_1\mathbf{B}_1\mathbf{R}_{g1}^{-1}\mathbf{B}_1^T\mathbf{P}_1 - \mathbf{P}_1\mathbf{A}_2 - \mathbf{A}_2^T\mathbf{P}_1 \tag{29}$$

$$\mathbf{Q}_{g2} = \mathbf{P}_1\mathbf{B}_1\mathbf{R}_{g2}^{-1}\mathbf{B}_1^T\mathbf{P}_1 \tag{30}$$

Step 3 (Feedback gain)

Finally, calculate the feedback gains as

$$\mathbf{K}_1 = -\mathbf{R}_1^{-1}\mathbf{B}_1^T\mathbf{P}_1 \tag{31}$$

$$\mathbf{K}_{g1} = -\mathbf{R}_{g1}^{-1}\mathbf{B}_1^T\mathbf{P}_1 \tag{32}$$

$$\mathbf{K}_{g2} = -\mathbf{R}_{g2}^{-1}\mathbf{B}_1^T\mathbf{P}_1 \tag{33}$$

The above three-step procedure is a kind of partial inverse LQR method that provides the desired hierarchical control structure represented by (23), since the choices of $\mathbf{Q}_{g1}$ and $\mathbf{Q}_{g2}$ are not completely free but restricted as in (29) and (30), respectively, which assure the optimal feedback gain belong to the desired class given by (23) as will be proved in the following proposition.

Proposition 1: Consider the linear time-varying interconnected system (15) with the matrices represented by (16) ~ (18). Assume that the pairs ($\mathbf{A}_1$, $\mathbf{B}_1$) and ($\mathbf{A}$, $\mathbf{B}$) are controllable and the positive semidefinite weighting matrices $\mathbf{Q}_1$ can be selected such that ($\mathbf{Q}_1^{1/2}, \mathbf{A}_1$) and (($\mathbf{Q}$')$^{1/2}$, $\mathbf{A}$) are observable where $\mathbf{Q}' := \mathbf{I}_N \otimes \mathbf{Q}_1 + \mathbf{\Gamma}_N \otimes \mathbf{Q}_{g1}$. Let $\mathbf{\Psi}_N$ be the positive semidefinite matrix, and the weighting matrices $\mathbf{Q}$, $\mathbf{R}$, and $\mathbf{S}$ are obtained as (24) ~ (26), where $\mathbf{R}_{g1}$, $\mathbf{R}_{g2}$, $\mathbf{Q}_{g1}$, and $\mathbf{Q}_{g2}$ are selected as in Step 2. Then, the optimal feedback gains are calculated as the formulae of (31) ~ (33).

See Appendix 3 for the detailed proof of the proposition.

6. Verification of the proposed H-LQR by simulations

6.1. Implementation of the slip ratio control based on H-LQR

Since the goal of this paper is controlling the wheel slip ratios such that they follow the reference values λ_i^*, the tracking errors are introduced as augmented sates, and the augmented dynamical model is defined as follows:

$$\dot{\bar{\mathbf{x}}}_i = \bar{\mathbf{A}}_1\bar{\mathbf{x}}_i + \bar{\mathbf{B}}_1\mathbf{u}_i + \sum_{j=1}^{N}\bar{\mathbf{A}}_2\bar{\mathbf{x}}_j + \bar{\mathbf{B}}_2\lambda_i^* \tag{34}$$

where

$$\bar{\mathbf{x}}_i = \begin{bmatrix} F_i & \lambda_i & e_i \end{bmatrix}^T,\ e_i = \int\left(\lambda_i - \lambda_i^*\right)dt$$

and the augmented matrices are expressed as follows in the driving mode:

$$\bar{\mathbf{A}}_1 = \begin{bmatrix} -\dfrac{1}{\tau_n} & \dfrac{D_n}{\tau_n} & 0 \\ -\dfrac{r_n}{J_n\omega_n} & -\dfrac{\dot{\omega}_n}{\omega_n} & 0 \\ 0 & 1 & 0 \end{bmatrix},\ \bar{\mathbf{B}}_1 = \begin{bmatrix} 0 \\ \dfrac{1}{J_n\omega_n} \\ 0 \end{bmatrix}$$

$$\bar{\mathbf{A}}_2 = \begin{bmatrix} 0 & 0 & 0 \\ -\dfrac{1}{mr_n\omega_n} & 0 & 0 \\ 0 & 0 & 0 \end{bmatrix},\ \bar{\mathbf{B}}_2 = \begin{bmatrix} 0 \\ 0 \\ -1 \end{bmatrix}$$

It is simple to check that the augmented model preserves the controllability of the original model. Then, the procedure in the previous section can be similarly applied to the augmented model as well. Using the proposed procedure, it is unnecessary to solve the large size Riccati equation (21). Instead, the control system only needs to solve the Riccati equation (27) for a local

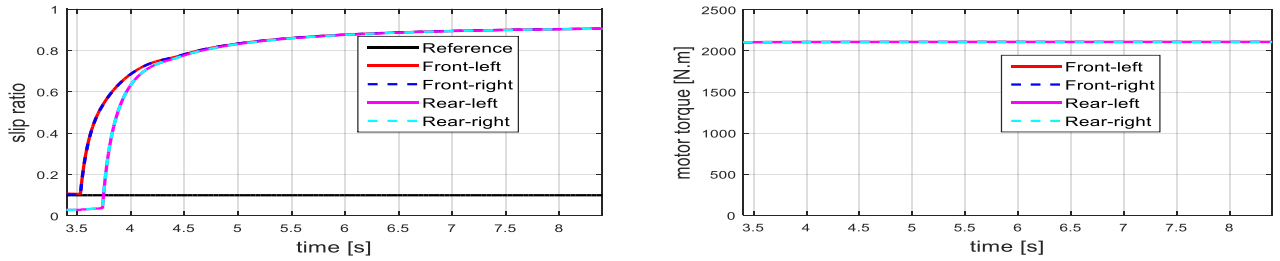

(a) Slip ratio (b) Motor torque

Fig.11. Simulation with flat road surface – Case 1: Without slip control.

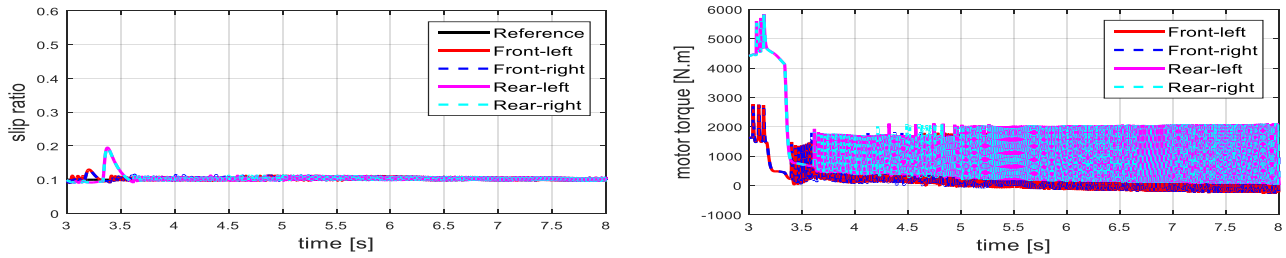

(a) Slip ratio (b) Motor torque

Fig.12. Simulation with flat road surface – Case 2(a): Sliding mode control (high gain).

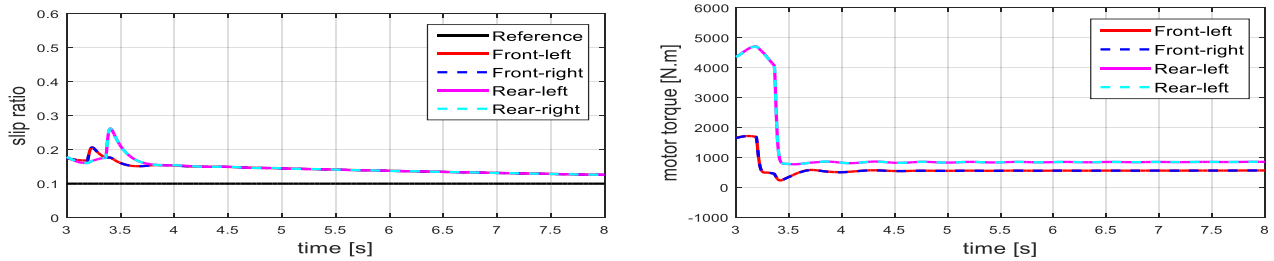

(a) Slip ratio (b) Motor torque

Fig.13. Simulation with flat road surface – Case 2(b): Sliding mode control (low gain).

subsystem. Therefore, the computational effort is considerably reduced. Theoretically speaking, equation (27) can be solved backwards in time. However, this algorithm is not really suitable for practical applications. In Appendix 4, following [36], an approximate solution of $\bar{P}_1$ is given such that the control gain can be updated at any control period.

Remark 5: The reference slip ratio depends on the road condition. There are many works on searching the optimal slip ratio by identifying the road surface's friction coefficient [37]. By focusing on controller design, this paper does not discuss such searching algorithm. In stead, this paper is to demonstrate the control performance of H-LQR.

The reference $\lambda^* = 0.1$ used in this paper is not a large number. It is not the optimal one, but safe enough for traction control on slippery surface. It is possible to set a smaller reference, for instance $\lambda^* = 0.05$, for the safer traction control. However this smaller reference will reduce the acceleration capability of the vehicle. With the same experiment condition as in this paper, the reference $\lambda^* = 0.2$ was used in [4], and the reference $\lambda^* = 0.1$ was used in [9].

6.2. Slip ratio control based on sliding-mode scheme

The effectiveness of the proposed H-LQR is demonstrably comparing it with the slip ratio control based on sliding-mode scheme proposed by Nam *et al* [4]. According to this method, the dynamics of slip ratio at the *i*th wheel is decoupled from other wheels as

$$\dot{\lambda}_i \approx \frac{\dot{v}_x}{v_x}\left(\lambda_i - 1\right) + \frac{v_x}{J_i r_i \omega_i^2}\left(T_i - r_i F_i\right) + d_i \tag{35}$$

where d_i is a lumped disturbance including terms related to driving resistances and parameter uncertainties. By using the sliding surface $\varphi = \lambda_i - \lambda_i^*$ with the reaching condition $\dot{\varphi} = -\beta\varphi - K_S \text{sign}(\varphi)$, and defining the Lyapunov function $L = \frac{1}{2}\varphi^2$, the control signal is obtained as

$$\begin{aligned} T_i = {} & r_i F_i + \frac{J_i \omega_i \dot{v}_x}{v_x} + \frac{J_i r_i \omega_i^2}{v_x}\lambda_i^* \\ & - \frac{J_i r_i \omega_i^2}{v_x}\beta\left(\lambda_i - \lambda_i^*\right) - \frac{J_i r_i \omega_i^2}{v_x} K_S \text{sign}\left(\lambda_i - \lambda_i^*\right) \end{aligned} \tag{36}$$

where the control parameters β and K_S are selected such that the derivative of the Lyapunov function is negative definite; F_i is obtained from driving force observer; and sign() is the expression of the signum function.

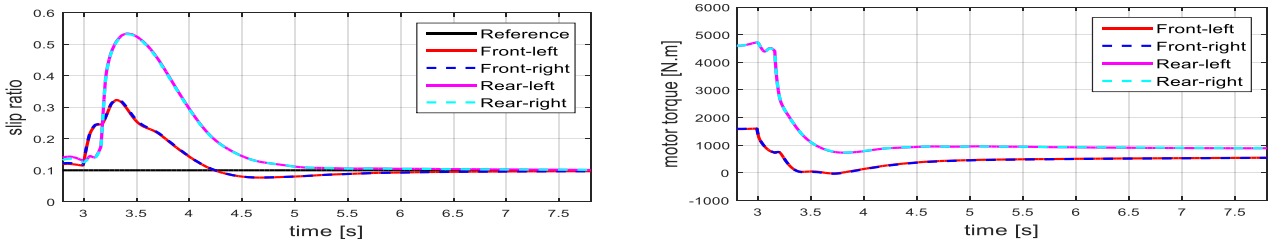

(a) Slip ratio (b) Motor torque

Fig.14. Simulation with flat road surface – Case 3(a): H-LQR (Computation period τ = 10 ms and $\Psi_4 = 0$).

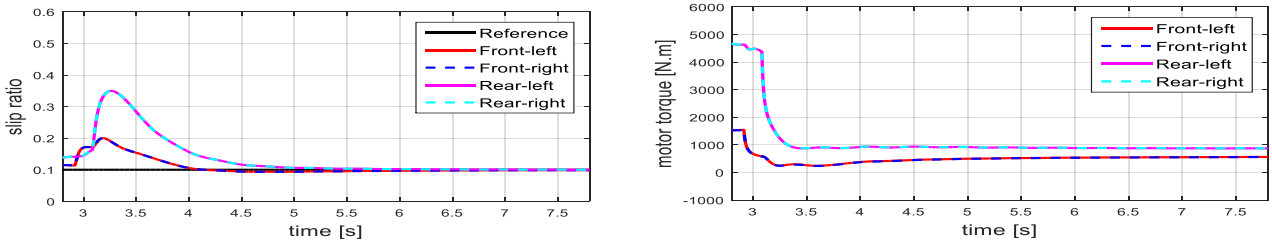

(a) Slip ratio (b) Motor torque

Fig.15. Simulation with flat road surface – Case 3(b): H-LQR (Computation period τ = 1 ms and $\Psi_4 = 0$).

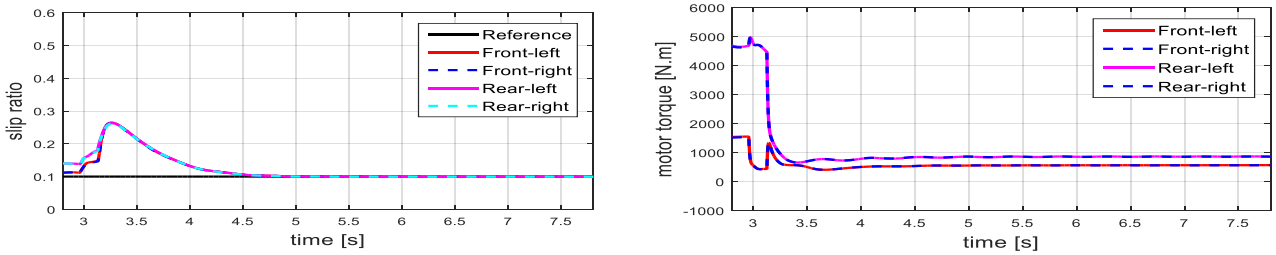

(a) Slip ratio (b) Motor torque

Fig.16. Simulation with flat road surface – Case 4: H-LQR (Computation period τ = 1 ms and $\Psi_4 \neq 0$).

6.3. Verification by simulations: Flat road surface

This paper considers a situation such that the vehicle accelerates with constant driving command and enters the slippery surface which is flat and uniform. The vehicle model and test condition are the same as *Motivating example 2* in Section 3. The desired value λ_i^* of the slip ratio on the slippery road is set to be 0.1. Simulation results are summarized in Figs. 11 - 16.

Case 1 - Without slip control (Fig. 11): The wheel slip ratios increase considerably since the vehicle enters the slippery surface. This phenomenon happens due to the reason that the wheel torques is maintained constantly on the low friction road. Case 1 is a fail example of vehicle traction.

Case 2 – Slip control based on sliding mode scheme proposed in [4] (Fig. 12 and Fig. 13): To utilize the advantage of IWM, the control signal is updated every 1 milli-second. In Case 2(a), for quickly suppressing the slip ratios, the high gains are selected as β = 200 and K_S = 13.5. As shown in Fig. 12, the trade-off cannot be avoided, although the wheel slip ratios are quickly suppressed. Transparently, the chattering phenomenon occurs with high frequency. This problem introduced bad influences to both the driving comfort and the motor drive systems. In Case 2(b), the control gains are reduced to as β = 50 and K_S = 6.5 to smooth the motor torque. However, as shown in Fig. 13, the tracking performance of slip ratio control is degraded. This is a trade-off that everyone has to accept when using the sliding mode control.

Case 3 – Slip control based on H-LQR with $\mathbf{\Psi}_4 = 0$ (Fig. 14 and Fig. 15): In this test, the coordination matrix $\mathbf{\Psi}_4$ is set to zero, and other weighting matrices are set as

$$\bar{\mathbf{Q}}_1 = diag\{1\times10^{-4}, 2\times10^{2}, 4\times10^{3}\}$$

$$\bar{\mathbf{R}}_1 = 4\times10^{-4},\ \bar{\mathbf{R}}_{g1} = 1\times10^{-1},\ \bar{\mathbf{R}}_{g2} = 1$$

In our slip ratio control system, $\bar{\mathbf{A}}_1$ and $\bar{\mathbf{B}}_1$ are time-varying matrices. Besides that, it is really hard to set a long final time t_f. The reason is that the road condition ahead or the length of the slippery surface cannot be known accurately in advance. However, during a short time interval, $\bar{\mathbf{A}}_1$ and $\bar{\mathbf{B}}_1$ can be seen as time-invariant matrices. For instance, it is possible to pay attention to the interval between time $t_0 = t$, and $t_f = t + \tau$ where τ is the control period. A solution of $\bar{\mathbf{P}}_1$ can be obtained using formula (50) in the Appendix 4, and then the control gains are calculated accordingly. In the next control period, $\bar{\mathbf{A}}_1$ and $\bar{\mathbf{B}}_1$ are updated with the measurement of wheel velocity, where the time-varying model is used, and $\bar{\mathbf{S}}_1$ can be set as $\bar{\mathbf{P}}_1$ in the

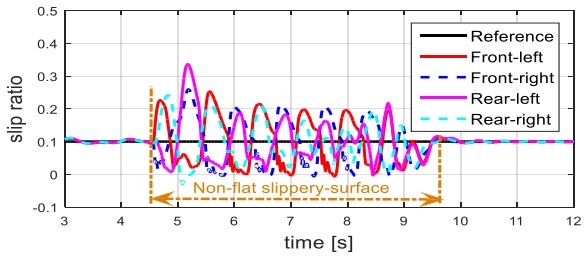

Fig.17. Simulation of H-LQR control with non-flat surface between 4.5 and 9.5 seconds.

previous control period. Consequently, a new solution of $\bar{\mathbf{P}}_1$ is obtained for calculating the new control gains. The procedure is repeated every control period until the vehicle passes the slippery surface.

Although the above procedure, which is a kind of receding horizon model predictive control, only gives a sub-optimal solution of the Riccati equation (27), it is quite convenient for practical applications. Since the size of system matrix $\bar{\mathbf{A}}_1$ and $\bar{\mathbf{B}}_1$ are only 3-by-3 and 3-by-1, respectively, formula (50) is calculated with small computational effort.

In this simulation, $\bar{\mathbf{P}}_1$ is updated at every computation period $\tau = 10$ milli-second or $\tau = 1$ milli-second. Fig. 14(a) shows that, nice slip ratio control is still achieved with $\tau = 10$ milli-second. However, slip ratio is suppressed faster with $\tau = 1$ milli-second, as demonstrated in Fig. 15(a). From this comparison, the shorter computation period is preferable. Thus, the computation period $\tau = 1$ milli-second is selected for conducting the experiment.

Case 4 – Slip control based on H-LQR with $\mathbf{\Psi}_4 \neq 0$ (Fig. 16). To deal with the unbalance between front and rear wheels due to load transfer during acceleration, the coordination matrix is not zero but $\mathbf{\Psi}_4^{front-rear}$ with $\varphi_{front} = \varphi_{rear} = 1$. The setting of other weighting matrices is similar to Case 3 with $\tau = 1$ milli-second.

As shown in Fig. 16, Case 4 can attain nice tracking performance of slip ratio with smooth motor torques. This means the driving comfort is preserved successfully. In Case 3 with $\tau = 1$ milli-second or $\tau = 10$ milli-second, there exists a larger gap between the front and rear slip ratios as the vehicle enters the slippery surface. In contrast, Case 4 shows a better consensus of four wheels' slip ratios. This means the introducing extra weighting matrix Ψ_N can improve the extra performance only by locally controlling the IWMs.

6.4. Verification by simulations: Non-flat road surface

To evaluate the performance of the proposed method, this sub-section examines the vehicle traction control on non-flat surface. The test course "Chassis twist road sine wave," was prepared similarly to the *Motivating example 3*. Slip ratio control based on H-LQR is designed similarly to the previous sub-section with $\tau = 1$ milli-second and $\mathbf{\Psi}_4 \neq 0$. As demonstrated in Fig. 17, better tracking performance is achieved in comparison with the *Motivating example 3* (Fig. 8). The results clarify the advantage of H-LQR by addressing the physical interaction in slip ratio control.

6.5. Summary

The simulation results clarify the advantages of the proposed system modeling and H-LQR control. By considering the wheel velocity as a time-varying parameter, the slip ratio dynamics can be modeled with linear state space equations. Thus, an innovation of glocal (global/local) control theory, namely the hierarchical LQR, can be utilized for slip ratio control. The design of H-LQR is simple, since the system can be normalized to a special class of linear interconnected system. With the H-LQR, it is not necessary to design the controller using nonlinear theory or Lyapunov stability. Thanks to the H-LQR, better traction performance was attained in comparison with the popular sliding mode control and PI control scheme. Moreover, using the H-LQR, not only local objective (wheel slip ratio) but also some extra purposes could be achieved globally.

7. Experimental verification of the proposed H-LQR

7.1. Experimental vehicle

In this study, experiments are conducted using the EV named "Super-capacitor COMS" developed in the authors' research group (Fig. 18(a)). A detailed explanation of the vehicle system was presented in our previous works [38]. The vehicle has four wheels but only two rear wheels are driven by IWMs. This means the number of agents is $N = 2$. The IWM is of IPMSM type, with the maximum power of 2kW. The motor drives and inverters are provided by Myway. The vehicle mass without the driver is $m = 400$ [kg]. The wheel moment of inertia is $J_i = J_n = 1.26$[kg.m^2] and the wheel radius is $r_i = r_n = 0.3$[m].

The vehicle is equipped with RTK-GPS receiver produced by Hemisphere, the gyroscopes, and the accelerometers. The vehicle velocity can be obtained through the fusion of GPS receiver, gyroscopes, and accelerometers. The encoders are installed at the wheels to measure the rotational speed. The heart of the system is a RT-Linux computer which processes the control algorithm and stores the experimental data. It can generate the control signals or sample the measurements at every 1 milli-second, which means that all the computation including solving the Riccati equation is done within 1 milli-second.

7.2. Experiment results

Experiments were conducted in Kashiwa campus of the University of Tokyo. The low friction plate made from polymer materials is cover with water to make the slippery surface, as shown in Fig. 18(b). The driver accelerates the vehicle from a starting point near by the slippery plate. He gives the maximum acceleration to the pedal, and this command is maintained constantly. Five test cases are performed, and the experimental results are shown in Figs. 19 - 23.

Notice: It is noticed that the times the vehicle enters the slippery-surface are not completely coincident. It depends on the time period from the moment that the driver starts the control program to the moment that the driver pressed the acceleration pedal. This time period is slightly different from test case to test case.

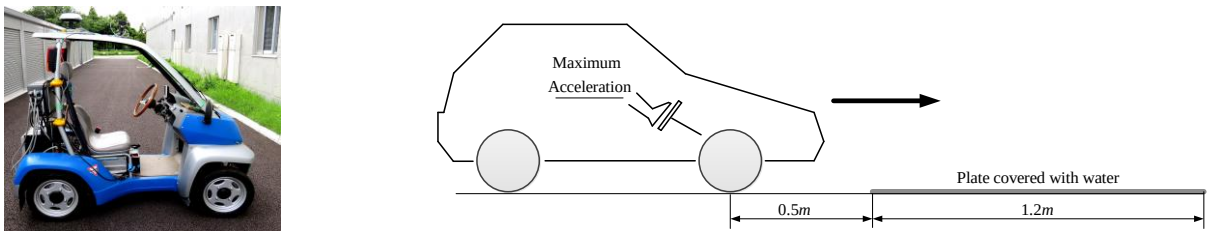

(a) Electric vehicle COMS. (b) Experiment setting.

Fig.18. Experimental system.

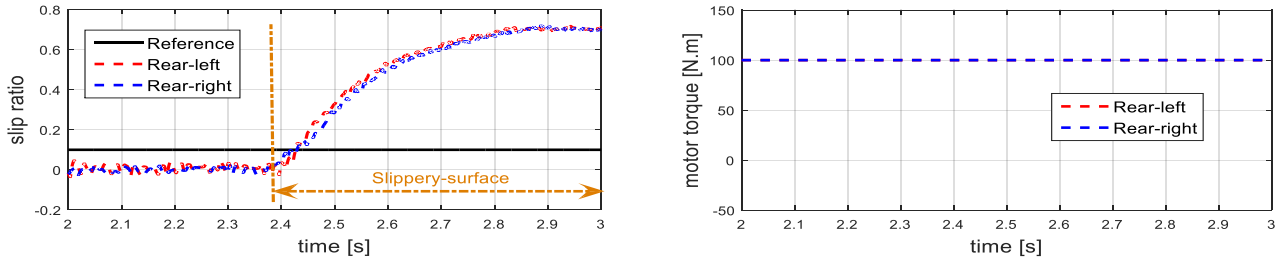

(a) Slip ratio (b) Motor torque

Fig.19. Experiment – Case 1: Without slip ratio control.

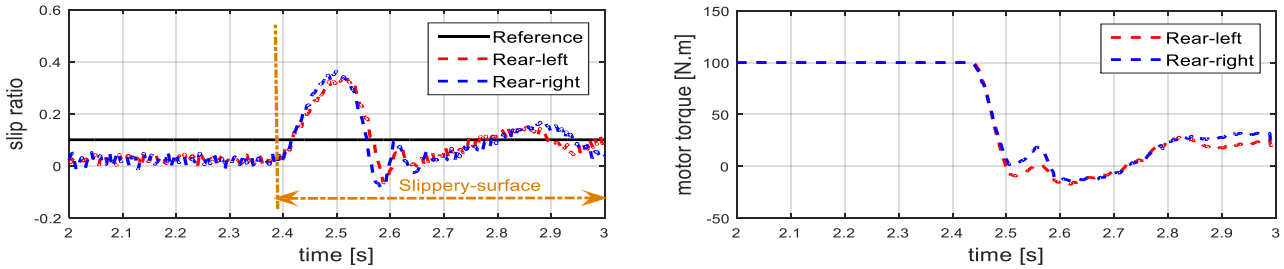

(a) Slip ratio (b) Motor torque

Fig.20. Experiment – Case 2: PI control.

Case 1 – Without slip control (Fig. 19): The slip ratios increase to 0.7 on the slippery surface, since the motor torque are maintained constantly.

Case 2 – Slip control by PI control scheme (Fig. 20). Similarly to the motivating example, the PI gains are calculated by placing the poles of the local subsystem as $-6 \pm 0.5j$ at the operating point $\omega_{o,i} = 13 rad/s$; $\dot{\omega}_{o,i} = 80 rad/s^2$. Unlike the results of Case 1, the motor torques are quickly reduced on the slippery surface, and hence the actual slip ratios track to the reference values. The PI control attains nice control performance as prediction by simulation, since the road surface is quite flat.

Case 3 – Slip control by model following control (or MFC) (Fig. 21). The detail of this method was presented in [9]. The key idea of MFC is that each wheel can be provided a MFC loop with the small-slip-nominal model J_{model}. For instance, with two driving wheels, J_{model} can be selected as follows with the small slip ratio λ^*:

$$J_{model} = J + \frac{mr^2}{2}\left(1-\lambda^*\right) \quad (37)$$

If the slip occurs, the actual wheel velocity increases immediately and considerably in comparison with the nominal model's wheel velocity. By feeding such velocity difference back to the motor current command, the motor torque is reduced quickly, as shown in Fig. 21. The MFC is a very rough approach for preventing the slip phenomenon, but it is very simple to implement. The actual slip ratios vibrate, instead of converging to λ^*.

Case 4 – Slip control by sliding mode scheme (Fig. 22). The control gains are set as $\beta = 150$ and $K_S = 10$. Although the slip ratio follows the desired value of 0.1, the chattering phenomenon happens. This phenomenon is undesirable for driving comfort and the motor drives system as mentioned before.

Case 5 – Slip control by H-LQR (Fig. 23). Unlike the simulation model, the experimental EV only has two IWMs in the rear wheels. This means $N = 2$. To balance the difference between the rear left and rear right agents, the coordination matrix $\boldsymbol{\Psi}_2^{left-right}$ is selected with $\varphi_{left} = \varphi_{right} = 0.5$. Thanks to H-LQR, the slip ratio quickly follows the desired value. Moreover, the chattering happened in Case 4 is eliminated. Thus, the traction safety and the driving comfort are successfully improved. Comparing with the slip ratio control by PI scheme in Case 2, Case 5 attains better consensus of the rear-left and rear-right wheel's slip ratios.

Again, the experiment results clarify the advances of the H-LQR for traction control of EV with in-wheel-motors. The sliding-mode-control seems to be very effective except the

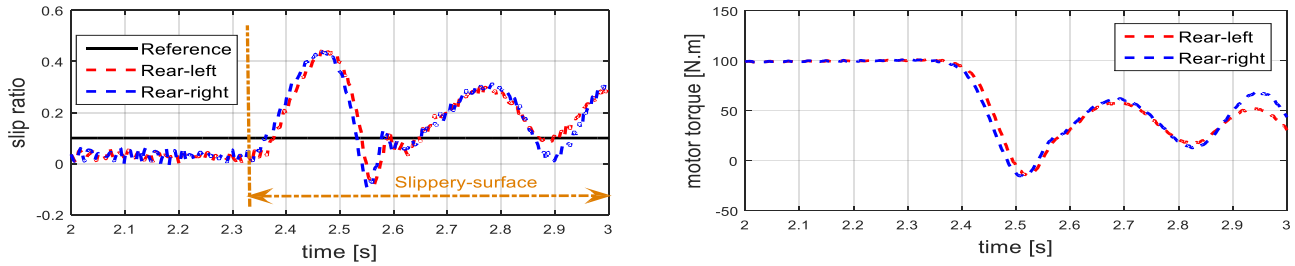

(a) Slip ratio (b) Motor torque

Fig.21. Experiment – Case 3: MFC.

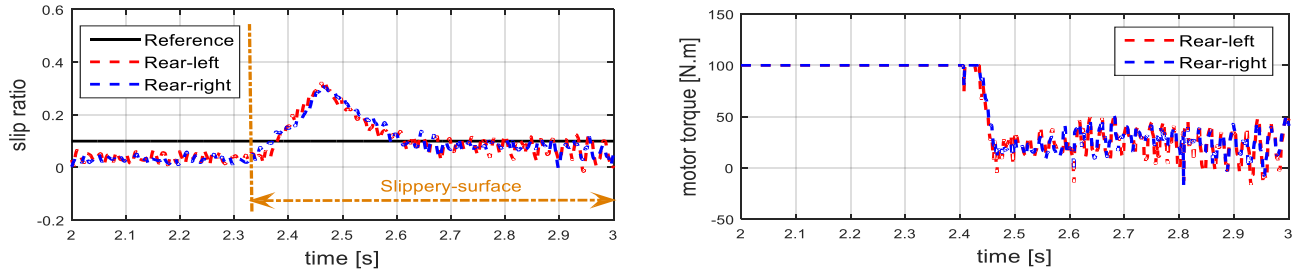

(a) Slip ratio (b) Motor torque

Fig.22. Experiment – Case 4: Sliding mode control.

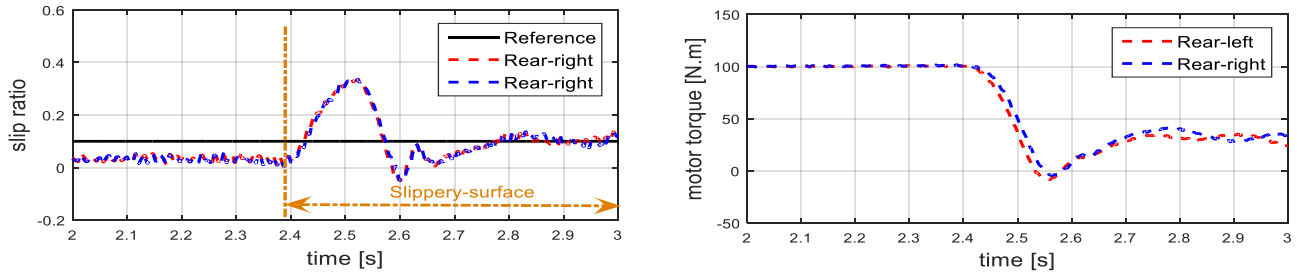

(a) Slip ratio (b) Motor torque

Fig.23. Experiment – Case 5: H-LQR control.

chattering problem: It is easy to implement, and its slip ratio suppression is quite fast. However, from the view point of glocal control theory [22], this design cannot assure the stability and optimality of the traction control system as a whole. In contrast, the H-LQR can capture the dynamics of the overall system. Moreover, it considerably reduces the cost of standard LQR for the sake of practical application.

7.3. Comparison of PI and H-LQR controllers

Observing the simulation and experiment results, the disadvantages of MFC and sliding mode control are clarified. While MFC is a rough anti-slip control method, sliding mode control suffers the chattering problem. Thus, this subsection only aims to compare the fixed-control-gain PI method with the proposed H-LQR method which updates the control gains at every control period. Since both methods are quite fast to suppress the slip ratio rising on the low friction surface, the following performance indicators are selected:

(i) The average of root mean square (RMS) of control error (ρ). The RMS of the control error at the i-th wheel is

$$\rho_i = \sqrt{\frac{1}{K_F - K_S + 1}\sum_{k=K_S}^{K_F}\left(\lambda_i(k) - \lambda_i^*\right)^2} \tag{38}$$

where λ_i^* is the reference slip ratio, and $\lambda_i(k)$ are measured in the time interval from K_S to K_F. Here, K_S is the control period that the vehicle enters the low friction surface, and the slip phenomenon starts to occur. On the other hand, K_F is the control period such that the vehicle completely gets out of the slippery surface. With N IWMs, the indicator ρ is calculated as

$$\rho_i = \frac{1}{N}\sum_{j=1}^{N}\rho_i \tag{39}$$

(ii) The average of overshoot in percentage (η). Let λ_i^p be the maximum slip ratio of the i-th wheel measured at its peak time since the vehicle enters the low friction surface. The indicator is calculated using the following formulae:

$$\eta_i = \frac{\lambda_i^p - \lambda_i^*}{\lambda_i^*}\times 100 \tag{40}$$

$$\eta = \frac{1}{N}\sum_{i=1}^{N}\eta_i \tag{41}$$

The H-LQR with suitable selection of interaction matrix $\boldsymbol{\Psi}_N$ is chosen for comparison. It is the H-LQR used in Case 4 of the simulation, and Case 5 of the above experiment. The results of ρ and η are summarized in TABLEs 3 and 4, respectively.

TABLE 3
AVERAGE RMS OF CONTROL ERROR OF ALL WHEELS

Test condition	PI	H-LQR
Simulation: flat surface	0.0839	0.0472
	(Fig.7)	(Fig. 16)
Simulation: non-flat surface (4.5s ~ 9.5s)	0.0645	0.0110
	(Fig. 8)	(Fig. 17)
Experiment: flat surface	0.0917	0.0504
	(Fig. 20)	(Fig. 23)

TABLE 4
AVERAGE OF OVERSHOOT OF ALL WHEELS

Test condition	PI	H-LQR
Simulation: flat surface	308.05%	164.8%
	(Fig.7)	(Fig. 16)
Experiment: flat surface	345.45%	238.45%
	(Fig. 20)	(Fig. 23)

H-LQR is shown to be better than PI method in term of RMS of control error. If the experiment or simulation are conducted with the flat surface, ρ(H-LQR) is approximately 1.8 times smaller than ρ(PI). The simulation with non-flat surface shows that ρ(H-LQR) is nearly 5.9 times smaller than ρ(PI). Due to the limitation of infrastructure as well as the safety purpose, the experiment on non-flat surface was not conducted as in Carsim simulation. However, with the proper treating of physical interaction, H-LQR is expected to attain finer control accuracy than that of PI method in actual driving conditions. Besides that, H-LQR is shown to have smaller overshoot in comparison with PI method. From TABLE 4, η(H-LQR) is about 1.9 times smaller than η(PI) in simulation, and 1.4 times smaller in experiment. The overshoot was not calculated for the test on non-flat surface (Fig. 8 and Fig. 17). This test is only to evaluate the influence of road surface's flatness to the steady state of slip ratio control.

8. Conclusions

This paper has two main contributions. Firstly, the paper clarifies the necessary of capturing the physical interaction in vehicle dynamics modelling. Secondly, the paper proposes a new method for the slip ratio control of EV driven by in-wheel-motors. The proposed method is based on hierarchical LQR which has been shown to be simple, systematic, and effective. Thanks to the H-LQR, instead of using the nonlinear control or linearization control schemes, it is possible to use the linear control scheme for time varying system. The design burden does not depend on the number of the wheels, since the control system only has to solve the single Riccati equation at the sub-system level, and then the control gains are obtained suitably thanks to the special structure of the slip ratio dynamics. Besides that, the interconnected model proposed in this paper can be used not only for wheel slip ratio control but also for any other traction control scheme summarized in TABLE 1. Another merit of the H-LQR is that some other extra objectives can be addressed by suitably selecting the coordination matrix.

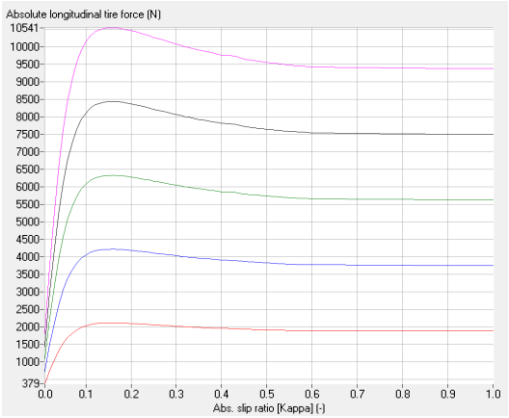

Fig.24. Nonlinear relationship between driving force (vertical axis) and slip ratio (horizontal axis).

The effectiveness of the proposed slip ratio control has been evaluated by both simulations and experiments. The method can maintain the safety traction and driving comfort, since it does not face with chattering phenomenon as seen in sliding mode control. In future works, the combination of this H-LQR based slip ratio control with other higher level motion control will be investigated. Besides that, an experiment with μ-split road surface and/or braking mode is a possible way to evaluate the performance of $\mathbf{\Psi}_N$.

Acknowledgement

This work was supported in part by the Ministry of Education, Culture, Sports, Science and Technology in Japan through Grant-in-Aid for Scientific Research (S) No. 16H06303.

Appendix 1: Nonlinear driving force model

Fig. 24 gives an example of the nonlinear relationship between the driving force and slip ratio at different vertical forces. The data, which belongs to the "Typical large vehicle Fx" in the Carsim Library, is calculated for the road surface with the friction coefficient μ = 0.9.

Appendix 2: A strategy for estimating the slip ratio

This Appendix briefly introduces a method for obtaining the slip ratio through a hierarchical estimator shown in Fig. 25. In the lower-layer, the *i*th slip ratio is estimated as

$$\dot{\hat{\lambda}}_i = -\frac{\dot{\omega}_i}{\omega_i}\hat{\lambda}_i + \frac{1}{J_i\omega_i}T_i - \frac{r_i}{J_i\omega_i}\hat{F}_i - \frac{1}{mr_i\omega_i}\sum_{j=1}^{N}\hat{F}_j + K_{li}\left(\lambda_{hi} - \hat{\lambda}_i\right) \quad (42)$$

where $\hat{F}_i$ is obtained from the local DOB expressed in Fig. 8; and $\hat{F}_j$,with $j \neq i$, is shared from other local estimators. The virtual measurement λ_{hi} is calculated through the estimated vehicle velocity $\hat{v}_h$ distributed from the upper-layer. The estimation gain K_{li} is computed at every control period by a standard Kalman filter algorithm. Each local estimator gives an estimated vehicle velocity $\hat{v}_{li}$ calculated from $\hat{\lambda}_i$ and ω_i. Then, the aggregated signal from lower-layer to upper-layer is

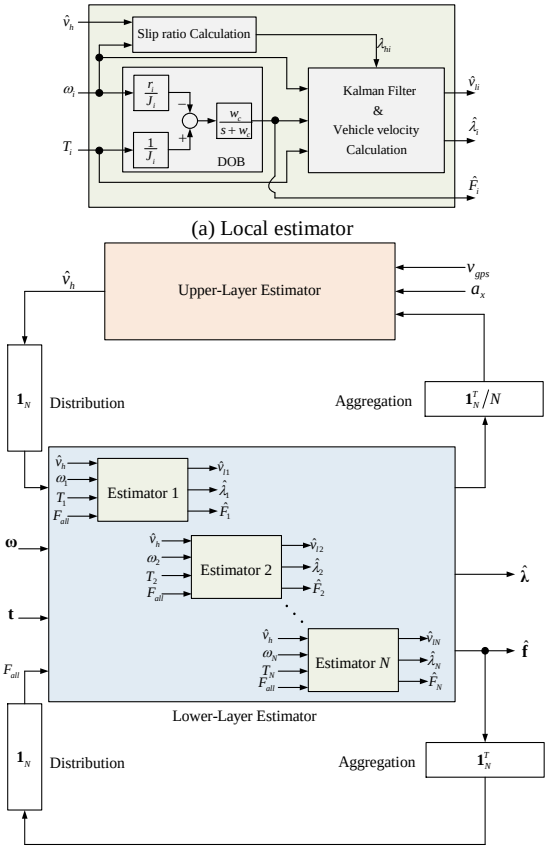

(a) Local estimator

(b) Hierarchical structure of the estimation

Fig. 25. Hierarchical estimation of slip ratio.

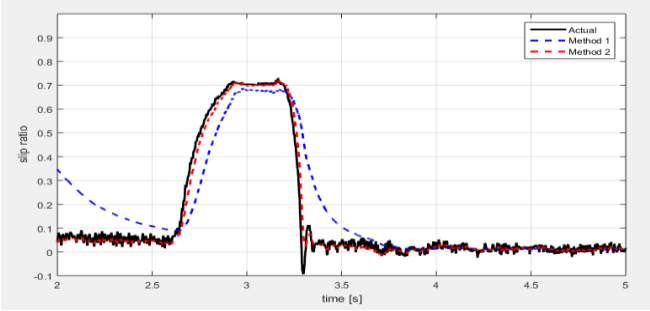

Fig. 26. Estimation results of rear-left wheel (Experiment).

$$\hat{v}_l = \frac{1}{N}\sum_{i=1}^{N}\hat{v}_{li} \tag{43}$$

The upper-layer estimator is to attain the estimated velocity $\hat{v}_h$ as follows:

$$\begin{pmatrix}\dot{\hat{v}}_h\\ \dot{\hat{d}}\end{pmatrix} = \begin{pmatrix}0 & 1\\ 0 & 0\end{pmatrix}\begin{pmatrix}\hat{v}_h\\ \hat{d}\end{pmatrix} + \begin{pmatrix}1\\ 0\end{pmatrix}a_x + \begin{pmatrix}K_{hv}^{l} & K_{hv}^{gps}\\ K_{hd}^{l} & K_{hd}^{gps}\end{pmatrix}\begin{pmatrix}\hat{v}_l - \hat{v}_h\\ v_{gps} - \hat{v}_h\end{pmatrix} \tag{44}$$

where $\hat{d}$ is the estimated accelerometer bias and v_{gps} is the vehicle velocity given by GPS receiver. The estimation gains are obtained from standard Kalman filter algorithm. At the estimation periods such that GPS signal is poor or unavailable, the corresponding gains $\{K_*^{gps}\}$ are set to zero.

An experimental verification of the hierarchical estimator is demonstrated in Fig. 26. Method 1 was proposed in [34]. This method is designed based on the local dynamics of slip ratio with the measurement of vehicle acceleration. If the accelerometer is corrupted by noise and bias, Method 1 provides poor slip ratio estimation. In contrast, the proposed method (namely, Method 2) can quickly track the actual value with small error, thanks to its hierarchical configuration. Thus, the proposed estimation can be used in real-time traction control as a safety index. The details of the estimation algorithm will be presented in our future works.

Appendix 3: Proof of the Proposition 1

The assumptions of controllability and observability are obvious for LQR design. According to Nguyen *et al*, the adding of the positive semidefinite term $\mathbf{\Psi}_N \otimes \mathbf{Q}_{g2}$ does not break the observability of the pair $((\mathbf{Q}')^{1/2}, \mathbf{A})$ [25]. Therefore, the weighting matrix $\mathbf{Q}_1$ can be selected such that both $(\mathbf{Q}_1^{1/2}, \mathbf{A}_1)$ and $(\mathbf{Q}^{1/2}, \mathbf{A})$ are observable. Consequently, differential Riccati equation (21) has a unique positive definite solution if $\mathbf{P}_f$ is positive.

Let suppose $\mathbf{P}$ has a block diagonal structure as $\mathbf{P} = \mathbf{I}_N \otimes \mathbf{P}_1$, since the boundary condition satisfies

$$\mathbf{P}_f = \mathbf{I}_N \otimes \mathbf{P}_{1f} = \mathbf{I}_N \otimes \mathbf{H}_1 = \mathbf{H} \tag{45}$$

Under this assumption, it can be seen from (27), (29), and (30) that

$$\begin{aligned}&\dot{\mathbf{P}} + \mathbf{P}\mathbf{A} + \mathbf{A}^T\mathbf{P} - \mathbf{P}\mathbf{B}\mathbf{R}^{-1}\mathbf{B}^T\mathbf{P} + \mathbf{Q}\\ &= \mathbf{I}_N \otimes \left[\dot{\mathbf{P}}_1 + \mathbf{P}_1\mathbf{A}_1 + \mathbf{A}_1^T\mathbf{P}_1 - \mathbf{P}_1\mathbf{B}_1\mathbf{R}_1^{-1}\mathbf{B}_1^T\mathbf{P}_1 + \mathbf{Q}_1\right]\\ &\quad + \mathbf{\Gamma}_N \otimes \left[\mathbf{Q}_{g1} - \mathbf{P}_1\mathbf{B}_1\mathbf{R}_{g1}^{-1}\mathbf{B}_1^T\mathbf{P}_1 + \mathbf{P}_1\mathbf{A}_2 + \mathbf{A}_2^T\mathbf{P}_1\right]\\ &\quad + \mathbf{\Psi}_N \otimes \left[\mathbf{Q}_{g2} - \mathbf{P}_1\mathbf{B}_1\mathbf{R}_{g2}^{-1}\mathbf{B}_1^T\mathbf{P}_1\right] = \mathbf{0}\end{aligned} \tag{46}$$

is satisfied. This implies that the unique solution of (21) has a block diagonal structure represented by $\mathbf{P} = \mathbf{I}_N \otimes \mathbf{P}_1$ for all t and that the optimal feedback gain is obtained as

$$\begin{aligned}&\mathbf{K} = -\mathbf{R}^{-1}\mathbf{B}^T\mathbf{P}\\ &= -\left(\mathbf{I}_N \otimes \mathbf{R}_1^{-1} + \mathbf{\Gamma}_N \otimes \mathbf{R}_{g1}^{-1} + \mathbf{\Psi}_N \otimes \mathbf{R}_{g2}^{-1}\right)\left(\mathbf{I}_N \otimes \mathbf{B}_1\right)\left(\mathbf{I}_N \otimes \mathbf{P}_1\right)\\ &= \mathbf{I}_N \otimes \left(-\mathbf{R}_1^{-1}\mathbf{B}_1^T\mathbf{P}_1\right) + \mathbf{\Gamma}_N \otimes \left(-\mathbf{R}_{g1}^{-1}\mathbf{B}_1^T\mathbf{P}_1\right) + \mathbf{\Psi}_N \otimes \left(-\mathbf{R}_{g2}^{-1}\mathbf{B}_1^T\mathbf{P}_1\right)\end{aligned} \tag{47}$$

Equation (47) shows that the feedback gain $\mathbf{K}$ has the structure as in (23), and $(\mathbf{K}_1, \mathbf{K}_{g1}, \mathbf{K}_{g2})$ are obtained as in the formula (31) ~ (33). This completes the proof.

Appendix 4: Approximate solution of Riccati equation

According to Wilson [36], if the system matrices are time-invariant, analytical solution of the Riccati equation can be obtained. Considering time-invariant dynamical system $\dot{\mathbf{x}} = \mathbf{A}_1\mathbf{x} + \mathbf{B}_1\mathbf{u}$ with the weighting matrices $\mathbf{Q}_1$ and $\mathbf{R}_1$, the Hamiltonian is defined as

$$\mathbf{\Phi} = e^{\mathbf{\Omega}t} = \begin{bmatrix}\mathbf{\Phi}_{11} & \mathbf{\Phi}_{12}\\ \mathbf{\Phi}_{21} & \mathbf{\Phi}_{22}\end{bmatrix} \text{ where } \mathbf{\Omega} = \begin{Bmatrix}\mathbf{A}_1 & -\mathbf{B}_1\mathbf{R}_1^{-1}\mathbf{B}_1^T\\ -\mathbf{Q}_1 & -\mathbf{A}_1^T\end{Bmatrix} \tag{48}$$

At time instant t, reference [36] gives the solution

$$\mathbf{P}_1(t) = \left(\mathbf{\Phi}_{22}\Big|_t^{t_f} - \mathbf{S}_1\mathbf{\Phi}_{12}\Big|_t^{t_f}\right)^{-1}\left(\mathbf{S}_1\mathbf{\Phi}_{11}\Big|_t^{t_f} - \mathbf{\Phi}_{21}\Big|_t^{t_f}\right) \tag{49}$$

where $\mathbf{\Phi}_{ij}\left|_{t}^{t_f}\right. = \mathbf{\Phi}_{ij}\left(t_f - t\right)$ and $\mathbf{S}_1$ represents the boundary condition. In many practical applications, it is possible to just consider $\mathbf{P}_1(t_0)$ given by

$$\mathbf{P}_1(t_0) = \left(\mathbf{\Phi}_{22}\left|_{t_0}^{t_f}\right. - \mathbf{S}_1\mathbf{\Phi}_{12}\left|_{t_0}^{t_f}\right.\right)^{-1}\left(\mathbf{S}_1\mathbf{\Phi}_{11}\left|_{t_0}^{t_f}\right. - \mathbf{\Phi}_{21}\left|_{t_0}^{t_f}\right.\right) \tag{50}$$

Remark 6: Since the symmetry of $\bar{\mathbf{P}}_1$ might be broken by numerical error, $\bar{\mathbf{P}}_1$ should be re-symmetrized by replacing it with $\frac{1}{2}\left[\bar{\mathbf{P}}_1 + \bar{\mathbf{P}}_1^T\right]$ at every control period.

References

[1] Y. Hori, "Future Vehicle Driven by Electricity and Control-Research on 4 Wheel Motored UOT Mach II," *IEEE Transactions on Industrial Electronics*, Vol. 51, No. 5, pp. 954-962, 2004.

[2] C. Geng, L. Mostefai, M. Denai, and Y. Hori, "Direct Yaw-Moment Control of an In-Wheel-Motored Electric Vehicle Based on Body Slip Angle Fuzzy Observer," *IEEE Transactions on Industrial Electronics*, Vol. 56, No. 5, pp. 1411-1419, 2009.

[3] H. Fujimoto and S. Harada, "Model-Based Range Extension Control System for Electric Vehicles With Front and Rear Driving-Braking Force Distributions," *IEEE Transactions on Industrial Electronics*, Vol. 62, No. 5, pp. 3245-3254, 2015.

[4] K. Nam, Y. Hori, and C. Lee: "Wheel Slip Control for Improving Traction-Ability and Energy Efficiency of a Personal Electric Vehicle," *Energies*, Vol. 8, No. 7, pp. 6820-6840, 2015.

[5] C. Lin and X. Cheng, "A Traction Control Strategy with an Efficiency Model in a Distributed Driving Electric Vehicle," *The Scientific World Journal*, Article ID 261085, 2014.

[6] B. Subudhi and S. S. Ge, "Sliding-Mode-Observer-Based Adaptive Slip Ratio Control for Electric and Hybrid Vehicles," *IEEE Transactions on Intelligent Transportation Systems*, Vol. 13, No. 4, pp. 1617-1626, 2012.

[7] H. He, J. Peng, R. Xiong, and H. Fan, "An Acceleration Slip Regulation Strategy for Four-Wheel Drive Electric Vehicles Based on Sliding Mode Control," *Energies*, Vol. 7, No. 6, pp. 3748-3763, 2014.

[8] M. Amodeo, A. Ferrara, R. Terzaghi, and C. Vecchio, "Wheel Slip Control via Second-Order Sliding-Model Generation," IEEE Transactions on Intelligent Transportation Systems, Vol. 11, Iss. 1, pp. 122-131, 2010.

[9] Y. Hori, Y. Toyoda, and Y. Tsuruoka, "Traction Control of Electric Vehicle: Basic Experimental Results Using the Test EV 'UOT Electric March'", *IEEE Transactions on Industry Applications*, Vol. 34, No. 5, pp. 1131-1138, 1998.

[10] V. Ivanov, D. Savitski, K. Augsburg, P. Barber, B. Knauder, and J. Zehetner, "Wheel Slip Control for All-wheel Drive Electric Vehicle with Compensation of Road Disturbance," *Journal of Terramechanics*, Vol. 61, pp. 1-10, 2015.

[11] K. Ohnishi, "A New Servo Method in Mechatronics," *Transactions of Japanese Society of Electrical Engineering*, Vol. 107-D, pp. 83-86, 1987.

[12] L. Li, S. Kodama, and Y. Hori, "Design of Anti-Slip Controller for an Electric Vehicle with an Adhesion Status Analyzer Based on the EV Simulator," *Asian Journal of Control*, Vol. 8, No. 3, pp. 261-267, 2006.

[13] H. Fujimoto, T. Saito, and T. Noguchi, "Motion Stabilization Control of Electric Vehicle Under Snowy Conditions Based on Yaw-Moment Observer," *Proceedings of the IEEE International Workshop on Advanced Motion Control*, pp. 35-40, 2004.

[14] D. Yin, S. Oh, and Y. Hori, "A Novel Traction Control for EV Based on Maximum Transmissible Torque Estimation," *IEEE Transactions on Industrial Electronics*, Vol. 56, No. 6, pp. 2086-2094, 2009.

[15] T. Suzuki and H. Fujimoto, "Slip Ratio Estimation and Regenerative Brake Control without Detection of Vehicle Velocity and Acceleration for Electric Vehicle at Urgent Brake-turning," *Proceedings of the 11th IEEE International Workshop on Advanced Motion Control*, pp. 273-278, 2010.

[16] J. Amada and H. Fujimoto, "Torque Based Direct Driving Force Control Method with Driving Stiffness Estimation for Electric Vehicle with In-wheel-motor," *Proceedings of the 38th Annual Conference on IEEE Industrial Electronics Society*, pp. 4904-4909, 2012.

[17] K. Maeda, H. Fujimoto, and Y. Hori: "Four-wheel Driving-force Distribution Method for Instantaneous or Split Slipery Roads for Electric Vehicle," Automatika, Vol. 54, No. 1, pp. 103-113, 2013.

[18] K. Maeda, H. Fujimoto, and Y. Hori, "Driving Force Control of Electric Vehicles with Estimation of Slip Ratio Limitation Considering Tire Side Slip," *Transactions of the Society of Instrument and Control Engineers*, Vol. 50, No. 3, pp. 259-265, 2014.

[19] L. Boulon, D. Hissel, A. Bouscayrol, O. Pape, M.-C., Pera, "Simulation Model of a Military HEV With a Highly Redundant Architecture," *IEEE Transactions on Vehicular Technology*, Vol. 59, Iss. 6, pp. 2654-2663, 2010.

[20] H. Shimizu, "Multi-purpose Electric Vehicle 'KAZ'," *IATSS Research*, Vol. 25, No. 2, pp. 96-97, 2001.

[21] Y. Suzuki, Y. Kano, and M. Abe, "A Study on Tyre Force Distribution Controls for Full Drive-By-Wire Electric Vehicle," *Vehicle System Dynamics*, Vol. 52, pp. 235-250, 2014.

[22] S. Hara, J. Imura, K. Tsumura, T. Ishizaki, and T. Sadamoto, "Glocal (Global/Local) Control Synthesis for Hierarchical Network System, *Proceedings of 2015 IEEE Conference on Control Applications*, pp.107-112, 2015.

[23] Y. Hori, T. H. Kim, and S. Hara, "Robust Stability Analysis of Gene-Protein Regulatory Networks with Cyclic Activation-Inhibition Interconnections," *Proceedings of the 7th Asian Control Conference*, pp. 1334-1339, 2009.

[24] W. Khaisongkram and S. Hara, "Performance and Analysis of Decentralized Cooperative Driving Under Non-Symmetric Bidirectional Information Architecture," *Proceedings of 2010 IEEE Conference on Control Applications*, pp. 2035-2040, 2010.

[25] DH. Nguyen and S. Hara, "Hierarchical Decentralized Stabilization for Networked Dynamical Systems by LQR Selective Pole Shift," *Proceedings of 19th IFAC World Congress*, pp. 5778-5783, 2014.

[26] D. Tsubakino, T. Yoshioka, and S. Hara, "An Algebraic Approach to Hierarchical LQR Synthesis for Large-Scale Dynamical Systems," *Proceedings of 9th Asian Control Conference*, pp. 1-6, 2013.

[27] T. Sadamoto, T. Ishizaki, and J. Imura, "Hierarchical Distributed Control for Networked Linear Systems," *Proceedings of 53rd IEEE Conference on Decision and Control*, pp. 2447-2452, 2014.

[28] B-M. Nguyen, S. Hara, and H. Fujimoto, "Stability Analysis of Tire Force Distribution for Multi-Actuator Electric Vehicles using Generalized Frequency Variable," *Proceedings of 2016 IEEE Conference on Control Applications*, pp. 91-96, 2016.

[29] B-M. Nguyen, H. Fujimoto, and S. Hara, "Glocal Motion Control System of In-wheel-motor Electric Vehicles Based on Driving Force Distribution," *Proceedings of the SICE International Symposium on Control Systems*, pp. 15-22, 2016.

[30] H. B. Pacejka, "Tyre and Vehicle Dynamics," Third Edition, *Published by SAE International and Butterworth Heinemann* with a Product Code of R-418, ISBN of 978-0-0809-7016-5, 2012.

[31] Mechanical Simulation homepage: https://www.carsim.com/.

[32] S. Hara, H. Tanaka, and T. Iwasaki, "Stability Analysis of Systems with Generalized Frequency Variables," *IEEE Transactions on Automatic Control*, Vol. 59, No. 2, pp. 313-326, 2014.

[33] G. Rill, "First Order Tire Dynamics," *Proceedings of III European Conference on Computational Mechanics Solids, Structures and Coupled Problems in Engineering*, 2006.

[34] K. Fuji and H. Fujimoto, "Traction Control Based on Slip Ratio Estimation Without Detecting Vehicle Speed for Electric Vehicle," *Proceedings of 2007 Power Conversion Conference*, pp. 688-693, 2008.

[35] D. M. Bevly, J. C. Gerdes, C. Wilson, and G. Zhang, "The Use of GPS Based Velocity Measurements for Improved Vehicle State Estimation," *Proceedings of the America Control Conference*, pp. 2538-2542, 2000.

[36] D. I. Wilson, "Advanced Control using MATLAB or Stabilising the Unstabilisable," Auckland University of Technology, 2015.

[37] H. Sado, S. Sakai, and Y. Hori, "Road Condition Estimation for Traction Control in Electric Vehicles," *Proceedings of IEEE International Symposium on Industrial Electronics*, pp. 973-978, 1999.

[38] B-M. Nguyen, Y. Wang, H. Fujimoto, and Y. Hori: "Lateral Stability Control of Electric Vehicle Based on Disturbance Accommodating Kalman Filter Using the Integration of Single Antenna GPS Receiver and Yaw Rate Sensor," *Journal of Electrical Engineering & Technology*, vol. 8, no. 4, pp. 899-910, 2013.

[39] Dinh Hoa Nguyen, Shinji Hara, "Hierarchical Decentralized Controller Synthesis for Heterogeneous Multi-Agent Dynamical Systems by LQR", *SICE Journal of Control, Measurement, and System Integration*, vol. 8, no. 4, pp. 295-302, 2015.